JOURNAL OF MATERIALS SCIENCE 28 (1993) 79–99

# Effect of interphase modulus and cohesive energy on the critical aspect ratio in short-fibre composites

L. MONETTE, M. P. ANDERSON, G. S. GREST
*Corporate Research Science Laboratory, Exxon Research and Engineering Company, Annandale, NJ 08801, USA*

The effect of interphase modulus and cohesive energy on critical fibre length in short-fibre reinforced brittle composites has been investigated employing computer simulation. The simulation consists of a two-dimensional computer model based upon a discrete network of grid points. Failure is defined in terms of an energy criterion, where the energy is calculated on the basis of a two- and three-body interaction between the grid points. Simulation results show that for a whisker-type fibre, a thick interphase (i.e. $A_i > A_f$ where $A$ represents the cross sectional area) with an elastic modulus less than that of the matrix in combination with an increased interphase toughness greatly reduce the critical aspect ratio, for both metal-matrix and ceramic-reinforced brittle polymer composites. The results also show a variation in the failure mode from tensile failure in the matrix to tensile and shear failure in the interphase as a function of the fibre–interphase modulus ratio. In particular, a significant increase in the load transfer efficiency in metal-matrix composites is found, for an interphase modulus $E_i$ less than the matrix modulus $E_m$. Better load transfer properties in metal-matrix composites cause the yield point to occur at higher values of applied strain, and hence may significantly increase the toughness (area under the stress–strain curve) for certain metal-matrix composites. The computer results are compared with the predictions of Cox's shear-lag theory as well as with a new theoretical development presented in this work. The new theory is found to provide a better description of the fibre and matrix stress distribution.

## 1. Introduction

The critical aspect ratio in fibre composites is a technologically important concept. A fibre whose aspect ratio is greater than the critical value strengthens the composite, while a fibre whose aspect ratio is less than the critical aspect ratio can degrade the composite. The interface between the fibre and the matrix is expected to play a critical part in load transfer since the load is communicated to the fibre through the interface. It is well known that the interface has a significant influence on the integrity of a composite and affects strength and Young's modulus in the fibre direction, as well as off-axis properties. Moreover, interfaces often have a dramatic effect on the toughness of fibre composites.

It has been long assumed that the longitudinal tensile strength of unidirectional fibre composites depends on the strength of the fibre and matrix by the rule of mixtures (e.g. [1]). Owen [2] observed that the longitudinal tension failure surface of surface-treated carbon fibre composites was brittle, while the untreated composites had a broom-like fracture surface. His observation suggested that the interface strength affects the failure mode and strength in the longitudinal tensile test, and this behaviour is not accounted for by the rule of mixtures. It is now known [3] that the failure of a composite involves not only the fracture of the load-bearing fibres and the matrix, but also involves the propagation of a set of cracks along the interfaces. It is therefore important to understand the properties of the interface and role in controlling fracture. Interfacial strength characterization and the study of adhesion mechanisms have consequently received a lot of attention.

The interfacial strength has been mainly characterized by the single-fibre "pull-out" test [4] pioneered by Favre [5], and used by that author [6] to determine the interfacial shear stresses for glass, carbon and Kevlar. Another established test is the single-fibre composite test or fragmentation test [7]. Using this test, Rao and Drzal [8] found a strong dependence of the interfacial shear strength on the bulk material matrix properties. Recently, two methods have been added to this series of tests: the microdebonding test [9] of Mandell *et al.* [10], where a shear-lag analysis including an interphase has been developed [11] and the microcompression or "push-in" test [12]. The experimental and analytical methods for the measurement of fibre–matrix interfacial shear strength have been reviewed in the literature [13–15]. In particular, Piggott [16] discussed the difference between the fragmentation test and the fibre pull-out test, i.e. fibre

0022–2461 

pull-out yields interfacial shear strength information as opposed to the fragmentation test which mostly provides frictional information. He also suggested that the criterion for interface failure in carbon–epoxy, glass–epoxy and glass–polyester resins is controlled by energy rather than by stress.

The various mechanisms of adhesion depend strongly on the nature of bonding, which in turn is influenced by the atomic arrangement and chemical properties of the fibre as well as by the molecular conformation of the matrix [3]. The chemical, physical and mechanical properties of various fibres and resin matrices have been discussed elsewhere [17]. The peel test [18] has been widely used to determine adhesion strength. Several elastic analyses of the peel test have been proposed in the literature (e.g. [19, 20]) where the peel force is directly related to the adhesive fracture energy. Recently, other analyses of the peel test have been given in which elastoplastic [21], viscoelastic [22] and inelastic [20] deformations are included. Adhesion has also been studied in relationship with the interfacial shear strength. Nardin and Schultz [23] observed a linear relationship between interfacial shear strength and the reversible work of adhesion. Asloun *et al.* [24] found that poor adhesion drastically reduced the effectiveness of load transfer from the matrix to the fibre. Most adhesion studies are primarily concerned with interfacial interactions (physical and chemical) and tend to neglect the matrix itself. Few experiments have been done in which the interfacial chemistry remains the same but the matrix properties are systematically varied [8].

The first theoretical analysis of load transfer was developed by Cox [25] and is referred to as the shear-lag analysis. The interfacial shear stress $\tau_i$ predicted by Cox's shear-lag theory is

$$\tau_i = \frac{\beta}{2}\left(\frac{E_f}{E_m}\right)\sigma_m\left(\frac{\sinh(\beta z/r_f)}{\cosh(\beta L/2r_f)}\right) \quad (1)$$

where $\beta$ is defined as

$$\beta = \left(\frac{2G_m}{E_f \ln(R/r_f)}\right)^{1/2} \quad (2)$$

Here $z$ is a coordinate running along the fibres length $-L/2 \leqslant z \leqslant L/2$, $E_f$ and $E_m$ are the elastic moduli of the fibre and the matrix, respectively; $G_m$ is the shear modulus of the matrix, $\sigma_m$ is the stress applied to the matrix at a distance $R$ from the fibre, $L$ is the length of the fibre and $r_f$ its radius. The square-root dependence of $\tau_i$ has been shown to hold in single-fibre pull-out tests [26]. Rosen [27] analysed the shear stress field along the fibres in a composite loaded in tension. His model consisted of a fibre surrounded by a matrix, which in turn is embedded within a composite material exhibiting average properties. The fibre and the average material are assumed to carry the load, while the matrix transmits shear stresses only. Dow [28] has evaluated the case where load is applied to both fibre and matrix. He obtained expressions for the tensile stress in the fibre and in the matrix close to the fibre–matrix interface and for the shear stress at the fibre–matrix interface, but with no intermediate interphase present. As the fibres are usually considered to have a uniform strength, Rosen [29], Kelly and Davies [30] and Tyson and Davies [31] introduced later some probabilistic aspects as well as allowed for plastic deformation of the matrix to take place. Piggott [32] proposed a theory in which the deformations at the fibre tips are perfectly plastic, while the deformations at the centre of the fibre are perfectly elastic. The above theoretical treatments are used for the analysis of most experimental results. Recently, Wagner and Eitan [33] have argued and experimentally verified that if the distance between the fibre flaws are assumed to follow a Poisson distribution, the statistical distribution of fragment lengths follows a shifted exponential distribution far from saturation and an approximately exponential distribution at the saturation limit. The saturation limit is defined in the context of the fragmentation test as the point at which no further fragmentation of the fibre occurs.

Some numerical work has also been undertaken to study the effect of interfaces in fibre composites. Two-dimensional [34, 35] and three-dimensional [36] finite-element analyses have been used. These methods assume zero interface thickness and uniform homogeneous matrix properties. Shih and Ebert [37] found numerically that an interface strong in shear increases the longitudinal tensile stress of the composite, especially in the case of a distribution in fibre failure strengths or a small coefficient of friction between the debonded fibre and the matrix. Termonia [38] found using a finite difference technique that fibre coating decreases the stress concentration and improves load transfer in the case of poor adhesion between the fibre and the matrix. He also found that adhesion has a strong influence on load transfer.

Recently, several researchers have suggested that the volume of material immediately surrounding the fibre is significantly different from the bulk matrix (for example, see Mäder and Freitag [4] for an illustration of the concept of interphase) and the importance of this interphase, or mesophase has been lately recognized [39, 40]. However, in spite of a large amount of experimental, theoretical and numerical effort, the properties of the interphase, as well as its role in composites, are not very well known or understood. This can be attributed in a large part to the fact that the results from the interfacial characterization tests described above are strongly dependent on many factors such as the specimen geometry, the fibre–matrix volume ratio, the fibre aspect ratio, sizing agents, etc. In particular, problems inherent in the fragmentation test have been discussed recently [41]. The ultimate goal is certainly to obtain an overall understanding of the role of mesophases in composites, i.e. to characterize this mesophase as well as to predict interfacial shear strengths as well as composite properties such as toughness, strength (load transfer), etc. from the fibre, matrix and mesophase properties.

In this work, we study the effect of interphase modulus and cohesive energy on the load transfer properties, namely the critical aspect ratio of elastic–brittle composites. Our study is based upon a shear-lag type analysis and computer simulations.

Computer simulations possess the advantage of being ideal, well-controlled environments. The computer model being considered consists of a coarse-grained system on a two-dimensional triangular lattice with perfect elastic forces between the nodes. The forces are derived from a Hamiltonian featuring two- and three-body interaction terms. The model has been described in detail elsewhere [42]. A cohesive energy parameter is incorporated into this study as a generalized fracture criterion [42], i.e. a bond is allowed to break if its energy $U$ is greater than or equal to the bond cohesive energy $U_b$. Such a criterion does not restrict the failure mode to pure tensile, shear or compression but allows one to access a failure surface as a function of tensile, shear and compression stresses as well as competition between these various failure modes. The cohesive energy parameter therefore enables us to make use of fracture information in our study of load transfer.

We present in section 2 a generalized theory of load transfer based on a shear-lag type analysis, which includes an interphase region between the matrix and the fibre. The theory of Cox [25], Dow [28], Rosen [27] and Tsai *et al.* [11] can be obtained from the above-mentioned theory as particular cases. We briefly describe in section 3 the computer model used in this study and discuss the simulation data. Section 4 summarizes the results, states our conclusions and briefly outlines future work.

## 2. Theory

The first part of this section outlines a general theory based on a shear-lag type approach for a three-phase composite material made of a single fibre plus an interphase region embedded in a soft matrix. All three phases carry both tensile and shear stresses.

Fig. 1a illustrates a cross-section in the $z$–$y$ plane of the system considered: a composite material in the dilute limit, in which a single fibre is embedded in a large volume of matrix, with an interphase region in between. $\tau_f$ is the shear stress at the fibre–interphase surface, $\tau_i$ the shear stress at the interphase–matrix surface and $\tau_m$ the shear stress in the matrix at a distance $r_m$. $r_f$ is the radius of the fibre, $r_i$ is the radius of the fibre plus interphase region and $r_m$ represents a distance chosen far away in the matrix. Fig. 1b is a sketch of the deformations in the composite material presented in Fig. 1a. The deformations are exaggerated for the sake of clarity, since the total strain applied to the composite material never exceed 2%. $\bar{r}_f$, $\bar{r}_i$ and $\bar{r}_m$ define a set of three surfaces where the shear stress is assumed to be zero in the fibre, interphase and matrix as shown in Fig. 1c, which illustrates a cross-section in the $x$–$y$ plane of the composite material. The forces exerted on the fibre, interphase and matrix within a distance $r = r_m$ are carried as tensile stresses only along these surfaces, i.e. $\sigma_f(z) = \sigma(z, \bar{r}_f)$, $\sigma_i(z) = \sigma(z, \bar{r}_i)$ and $\sigma_m(z) = \sigma(z, \bar{r}_m)$, and as shear stresses in between these surfaces.

The first equation is obtained by balancing the applied force on the fibre, interphase and matrix with the total applied force $F_{apl}$:

$$F_f + F_i + F_m = F_{apl}$$

or

$$A_f\sigma_f(z) + A_i\sigma_i(z) + A_m\sigma_m(z) = A_o\sigma_{apl} \quad (3)$$

where $A_f = \pi r_f^2$, $A_i = \pi(r_i^2 - r_f^2)$, $A_m = \pi(r_m^2 - r_i^2)$ and $A_o = A_f + A_i + A_m = \pi r_m^2$. The second set of equations is obtained by balancing the tensile and shear stresses:

$$\frac{dF(z, \bar{r}_f)}{dz} = A_f\frac{d\sigma_f(z)}{dz} = -2\pi r_f\tau_f(z) \quad (4)$$

$$\frac{dF(z, \bar{r}_i)}{dz} = A_i\frac{d\sigma_i(z)}{dz} = -2\pi[r_i\tau_i(z) - r_f\tau_f(z)] \quad (5)$$

$$\frac{dF(z, \bar{r}_m)}{dz} = A_m\frac{d\sigma_m(z)}{dz} = -2\pi[r_m\tau_m(z) - r_i\tau_i(z)] \quad (6)$$

where $\tau_f(z) \equiv \tau(z, r_f)$, $\tau_i(z) \equiv \tau(z, r_i)$ and $\tau_m(z) \equiv \tau(z, r_m)$. Note that in order for Equations 4–6 to be consistent with Equation 1, $\tau_m$ must be set to 0. This means that the distance $r_m$ must be chosen to be large enough so that beyond $r_m$ the material does not "feel" the effect of the fibre, i.e. for $r \geq r_m$ the displacement $u(z, r)$ is equal to the applied displacement.

The most general expressions for the shear stresses $\tau_f$ and $\tau_i$ are obtained in the following way: using the relations $r\tau(z, r) = r_f\tau(z, r_f)$ for $\bar{r}_f < r \leq r_f$ and $\tau(z, r) = G_f du(z, r)/dr$ where $G_f$ is the shear modulus of the fibre, and integrating

$$r_f\tau_f(z)\int_{r_f}^{\bar{r}_f}\frac{1}{r}dr = G_f\int_{u(z, r_f)}^{u(z, \bar{r}_f)}du$$

with the result

$$\tau_f(z) = \frac{G_f}{r_f}\left(\frac{u(z, \bar{r}_f) - u(z, r_f)}{\ln(\bar{r}_f/r_f)}\right) \quad (7)$$

Similarly, for $r_f \leq r < \bar{r}_i$

$$\tau_f(z) = \frac{G_i}{r_f}\left(\frac{u(z, \bar{r}_i) - u(z, r_f)}{\ln(\bar{r}_i/r_f)}\right) \quad (8)$$

and for $\bar{r}_i < r \leq r_i$

$$\tau_i(z) = \frac{G_i}{r_i}\left(\frac{u(z, \bar{r}_i) - u(z, r_i)}{\ln(\bar{r}_i/r_i)}\right) \quad (9)$$

and finally for $r_i \leq r < \bar{r}_m$

$$\tau_i(z) = \frac{G_m}{r_i}\left(\frac{u(z, \bar{r}_m) - u(z, r_i)}{\ln(\bar{r}_m/r_i)}\right) \quad (10)$$

Before we proceed to solve the above equations, we show how to recover some of the shear-lag theories in the literature.

### 2.1. Two-phase theories: fibre and matrix

#### *2.1.1. Cox shear-lag theory*

This theory [25] is concerned with one single fibre embedded in a softer matrix. The matrix carries both tensile and shear stresses. The tensile stress in the matrix is assumed to be constant and equal to the applied stress, which is a rather rough approximation.

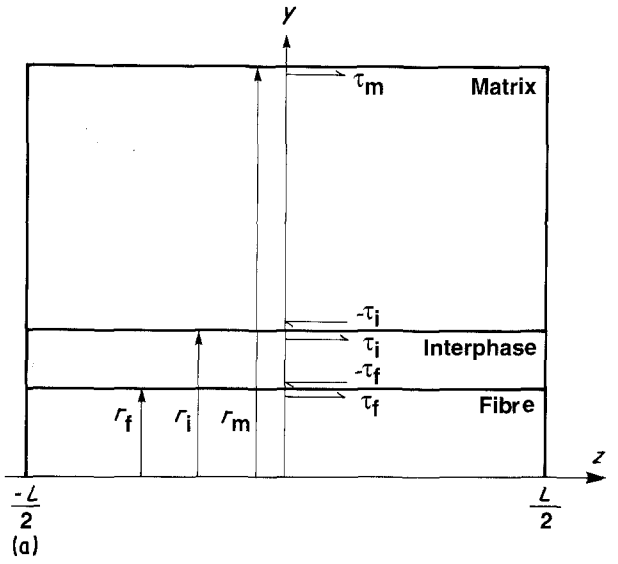


*Figure 1* (a) Sketch of $y$–$z$ cross-section of the composite material. Cylindrical symmetry is assumed with $r = (x^2 + y^2)^{1/2}$ therefore only the part $y \geq 0$ is shown. $r_f$ is the distance from the centre of the fibre to the boundary between the fibre and the interphase region, and $r_i$ the distance from the centre of the fibre to the boundary between the interphase region and the matrix. $r_m$ is defined as a distance far away in the matrix beyond which the stress (or strain) is equal to the applied stress (or strain). $\tau_f$ is the shear stress at the boundary between the fibre and the interphase region. $\tau_i$ is the shear stress at the boundary between the interphase region and the matrix while $\tau_m$ is the shear stress at a distance $r_m$ in the matrix. The fibre has a length $L$. (b) Sketch of the deformation (maximum 2%) in the composite material shown in Fig. 1a ($y$–$z$ cross-section). The shear stresses at these locations are consequently null: $\tau(z, \bar{r}_f) = \tau(z, \bar{r}_i) = \tau(z, \bar{r}_m) = 0$. $u'(z, \bar{r}_f)$, $u'(z, \bar{r}_i)$ and $u'(z, \bar{r}_m)$, are the displacements at $r = \bar{r}_f$, $\bar{r}_i$ and $\bar{r}_m$, and are respectively equal to $\sigma_f(z)/E_f$, $\sigma_i(z)/E_i$ and $\sigma_m(z)/E_m$. $u(z, r_f)$, $u(z, r_i)$ and $u(z, r_m)$ are the displacements at $r = r_f$, $r_i$ and $r_m$, with $r_f$, $r_i$ and $r_m$ defined in Fig. 1a. (c) Sketch of $x$–$y$ cross-section of the composite material. $r_f$, $r_i$ and $r_m$ are previously defined in Fig. 1a. It is assumed that the fibre, interphase and matrix carry the applied force as tensile stresses along the surfaces $r = \bar{r}_f$, $\bar{r}_i$ and $\bar{r}_m$ (dashed lines), and as shear stresses in between these surfaces.

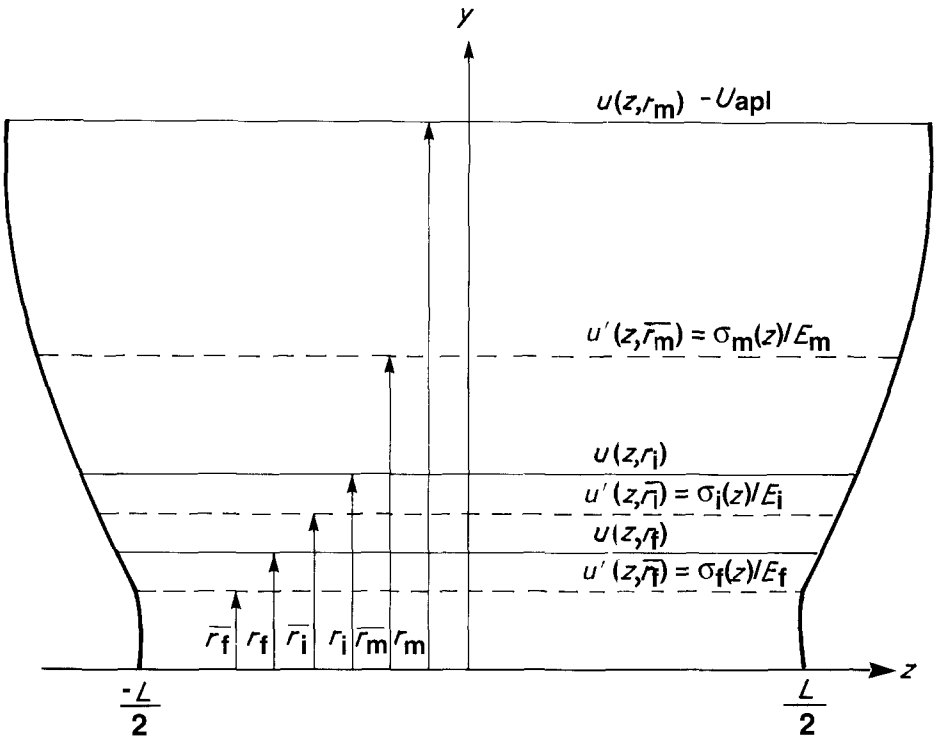


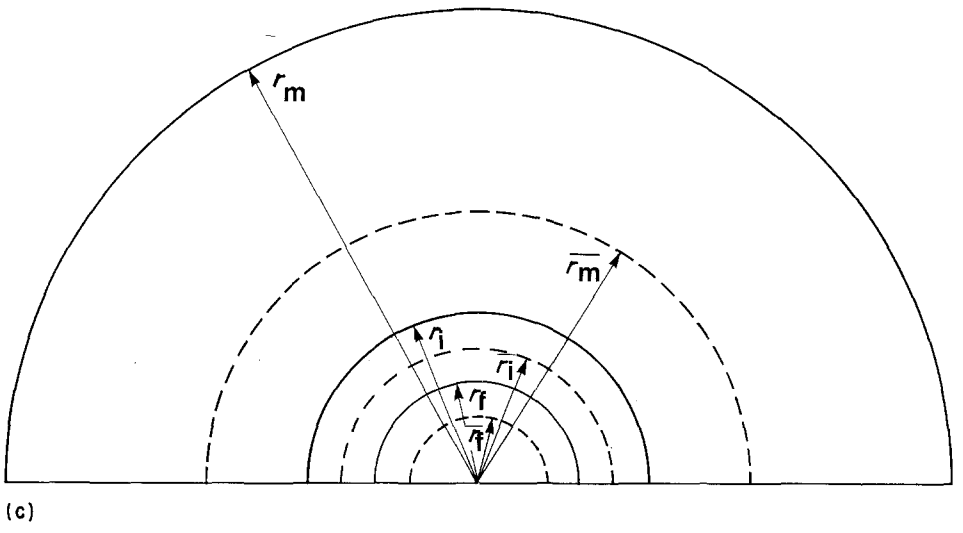

The fibre carries only tensile stress and this should be valid for whisker-like fibres:

(i) There is no interphase region, hence we discard Equation 5 and relabel $\tau_i \rightarrow \tau_f$ and $r_i = \bar{r}_i \rightarrow r_f$. Equations 8 and 9 are also discarded.

(ii) $\sigma_m = \sigma_{apl} \equiv$ constant, in which case Equation 6 gives $r_f \tau_f(z) = r_m \tau_m(z)$.

(iii) Since the forces are no longer balanced, Equation 3 must be discarded. $\tau_m$ is not necessarily null.

(iv) The fibre carries only tensile load: $\bar{r}_f = r_f$, and Equation 7 does not apply.

Equation 4 remains the same and $\tau_f$ is given by Equation 10:

$$\tau_f(z) = \frac{G_m}{r_f}\left(\frac{u_m(z) - u_f(z)}{\ln(r_m/r_f)}\right)$$

where $u_f(z) \equiv u(z, r_f)$, $u_m \equiv u(z, r_m)$ and for simplicity, $\bar{r}_m \rightarrow r_m$. One then obtains the well-known results for the fibre tensile stress $\sigma_f$ and interfacial shear stress $\tau_f$:

$$\sigma_f(z) = \frac{E_f \sigma_{apl}}{E_m}\left(1 - \frac{\cosh(\beta z/r_f)}{\cosh(\beta L/2r_f)}\right) \quad (11)$$

$$\tau_f(z) = \frac{\beta E_f \sigma_{apl}}{2E_m}\left(1 - \frac{\sinh(\beta z/r_f)}{\cosh(\beta L/2r_f)}\right) \quad (12)$$

and $\beta$ is given by Equation 2 with $r_m$ replacing $R$. Note that the boundary conditions $\sigma_f(-L/2) = \sigma_f(L/2) = 0$ have been used.

### 2.1.2. Dow shear-lag theory

This theory [28] is also for the case of a single fibre embedded in a softer matrix. The matrix carries both tensile and shear stresses, but the tensile stress in the matrix is allowed to have an axial dependence $\sigma_m \equiv \sigma_m(z)$. The fibre can carry tensile as well as shear stress, hence the Dow theory is not only restricted to whiskers:

(i) There is again no interphase region. Equation 5 is discarded and we relabel $\tau_i \rightarrow \tau_f$, $r_i \rightarrow r_f$, $\bar{r}_i \rightarrow \bar{r}_f$ and $G_i \rightarrow G_f$. Hence Equations 7–9 are equivalent.

(ii) The forces are balanced, and by Equation 3 $\tau_m = 0$.

Equation 4 remains the same, while Equation 5 becomes

$$\frac{dF(z, \bar{r}_m)}{dz} = A_m \frac{d\sigma_m}{dz} = 2\pi r_f \tau_f$$

Equations 7–9 become

$$\tau_f = G_f\left(\frac{u(z, r_f) - u(z, \bar{r}_f)}{r_f - \bar{r}_f}\right)$$

and Equation 10 becomes

$$\tau_f = G_m\left(\frac{u(z, \bar{r}_m) - u(z, r_f)}{\bar{r}_m - r_f}\right)$$

Dow takes the square root of the second moment of the mass distribution of the fibre and the matrix for $\bar{r}_f$ and $\bar{r}_m$:

$$\bar{r}_f = \left(\frac{\int r^2 \rho_f dV_f}{\int \rho_f dV_f}\right)^{1/2} = \left(\frac{r_f^2}{2}\right)^{1/2}$$

$$\bar{r}_m = \left(\frac{\int r^2 \rho_m dV_m}{\int \rho_m dV_m}\right)^{1/2} = \left(\frac{r_m^2 + r_f^2}{2}\right)^{1/2}$$

with $r = (x^2 + y^2)^{1/2}$ and uniform fibre and matrix densities $\rho_f = M_f/(2\pi r_f^2 L)$, $\rho_m = M_m/[2\pi(r_m^2 - r_f^2)L]$. $M_f$ is the mass of the fibre, $M_m$ is the mass of the matrix and $L$ is the sample length. He assumes furthermore that the deformation remains close to a straight line. This is true if $\bar{r}_f/r_f$, $r_f/\bar{r}_m \approx 1$ so $r_f \ln(\bar{r}_f/r_f) \approx -(r_f - \bar{r}_f) \equiv -\tilde{r}_f$, and $r_f \ln(\bar{r}_m/r_f) = \bar{r}_m - r_f = \tilde{r}_m$. Dow then obtains the following expressions for the tensile stress in the fibre and matrix:

$$\sigma_f(z) = \frac{A_o \sigma_{apl} E_f}{A_f E_f + A_m E_m}\left(1 - \frac{\cosh(\lambda z/r_f)}{\cosh(\lambda L/2r_f)}\right) \quad (13)$$

$$\sigma_m(z) = \frac{A_o \sigma_{apl}}{A_m(A_f E_f + A_m E_m)} \times \left(A_f E_f \frac{\cosh(\lambda z/r_f)}{\cosh(\lambda L/2r_f)} + A_m E_m\right) \quad (14)$$

$$\tau_f(z) = \frac{\lambda}{2}\left(\frac{A_o \sigma_{apl} E_f}{A_f E_f + A_m E_m}\right)\frac{\sinh(\lambda z/r_f)}{\cosh(\lambda L/2r_f)} \quad (15)$$

$$\lambda = \left[2\pi r_f^3\left(\frac{G_m G_f}{\tilde{r}_f G_m + \tilde{r}_m G_f}\right) \times \left(\frac{1}{A_f E_f} + \frac{1}{A_m E_m}\right)\right]^{1/2} \quad (16)$$

The following boundary conditions have been used: $\sigma_f(-L/2) = \sigma_f(L/2) = 0$ and $\sigma_m(-L/2) = \sigma_m(L/2) = A_o \sigma_{apl}/A_m$.

## 2.2. Three-phase theories: fibre, interphase and matrix

### 2.2.1. The theory of Tsai, Arocho and Gause

Tsai *et al.* [11] developed this theory for their fibre pull-out experiments; it is a generalization of Cox's shear-lag theory for which an interphase is added. The interphase and the matrix carry both tensile and shear stresses and the tensile stresses are assumed to be constant. The fibre carries only tensile stress:

(i) $\sigma_m = \sigma_{apl} \equiv$ constant and from Equation 6, $r_i \tau_i = r_m \tau_m$.

(ii) $\sigma_i \equiv$ constant which gives $r_i \tau_i = r_f \tau_f$ from Equation 5.

(iii) Since the forces are no longer balanced, Equation 3 must be discarded and $\tau_m \neq 0$.

(iv) $\bar{r}_f = r_f$, $\bar{r}_i = r_i$ and $\bar{r}_m = r_m$; hence Equations 7 and 9 are also discarded.

Equation 4 remains, while Equation 8 becomes

$$\tau_f(z) = \frac{G_i}{r_f}\left(\frac{u(z, r_i) - u(z, r_f)}{\ln(r_i/r_f)}\right)$$

and Equation 10 becomes

$$\tau_i(z) = \frac{G_m}{r_i}\left(\frac{u(z, r_m) - u(z, r_i)}{\ln(r_m/r_i)}\right)$$

One can solve for $\sigma_f(z)$ and $\tau_f(z)$ to obtain

$$\sigma_f(z) = \frac{E_f \sigma_{apl}}{E_m}\left(1 - \frac{\cosh(\alpha z/r_f)}{\cosh(\alpha L/2r_f)}\right) \quad (17)$$

$$\tau_f(z) = \frac{\alpha E_f \sigma_{apl}}{2E_m}\left(\frac{\sinh(\alpha z/r_f)}{\cosh(\alpha L/2r_f)}\right) \quad (18)$$

where

$$\alpha = \left(\frac{2G_i G_m}{E_f[G_m \ln(r_i/r_f) + G_i \ln(r_m/r_i)]}\right)^{1/2} \quad (19)$$

with $\tau_i(z) = \tau_f(z) r_f/r_i$ and $\tau_m(z) = \tau_f(z) r_f/r_m$. The boundary conditions $\sigma_f(-L/2) = \sigma_f(L/2) = 0$ have been used again in this case.

### 2.2.2. The shear-lag based approach of Rosen

This theory [27] was originally for the case of a fibre (f) embedded in a matrix (m) which in turn is embedded in a phase (a) displaying the average properties of the composite material. For the purposes of a single fibre with an interphase embedded in a matrix, we relabel the indices m and a to i and m. The fibre and the average material carry tensile stresses only. The interphase can carry both tensile and shear stresses, but the tensile stress is assumed constant or null:

(i) The forces are balanced, and by Equation 3 $\tau_m = 0$.

(ii) $\sigma_i \equiv$ constant, or is even null, according to the hypothesis that only the matrix and the fibre carry tensile load. By Equation 5, $r_f\tau_f = r_i\tau_i$ with $\bar{r}_i = r_i$. Consequently, Equations 9 and 10 are discarded.

(iii) The fibre does not carry shear stress. $\bar{r}_f = r_f$ and Equation 7 is discarded.

(iv) $E_m du(z, r_i)/dz = \sigma_m = \sigma_{apl} \equiv$ constant.

Equation 4 remains the same and Equation 8 becomes

$$\tau_f(z) = \frac{G_i}{r_f}\left(\frac{u(z, r_i) - u(z, r_f)}{\ln(r_i/r_f)}\right)$$

and one finally obtains

$$\sigma_f(z) = \frac{2G_i \sigma_{apl} r_m^2}{\mu^2 E_m \ln(r_i/r_f)(r_m^2 - r_i^2)} \times\left(1 - \frac{\cosh(\mu z/r_f)}{\cosh(\mu z L/2r_f)}\right) \quad (20)$$

$$\tau_f(z) = \frac{G_i \sigma_{apl} r_m^2}{\mu E_m \ln(r_i/r_f)(r_m^2 - r_i^2)}\left(\frac{\sinh(\mu z/r_f)}{\cosh(\mu L/2r_f)}\right) \quad (21)$$

where

$$\mu = \left\{\frac{2G_i}{E_f \ln(r_i/r_f)}\left[1 + \frac{E_f}{E_m}\left(\frac{r_f^2}{r_m^2 - r_i^2}\right)\right]\right\}^{1/2} \quad (22)$$

and $\sigma_f(-L/2) = \sigma_f(L/2) = 0$.

### 2.2.3. General solution

We now solve for $\sigma_i$, $\sigma_f$, $\sigma_m$, $\tau_f$ and $\tau_i$ in the general case, with no other assumption than $\tau_m = 0$. We use Equations 7 and 8 to obtain an expression for $u(z, r_f)$:

$$u(z, r_f) = \frac{G_f \ln(\bar{r}_i/r_f) u(z, \bar{r}_f) + G_i \ln(r_f/\bar{r}_f) u(z, \bar{r}_i)}{G_f \ln(\bar{r}_i/r_f) + G_i \ln(r_f/\bar{r}_f)} \quad (23)$$

and Equations 9 and 10 to obtain an expression for $u(z, r_i)$:

$$u(z, r_i) = \frac{G_i \ln(\bar{r}_m/r_i) u(z, \bar{r}_i) + G_m \ln(r_i/\bar{r}_i) u(z, \bar{r}_m)}{G_i \ln(\bar{r}_m/r_i) + G_m \ln(r_i/\bar{r}_i)} \quad (24)$$

Substituting Equations 23 and 24 into Equations 7 and 9 for $\tau_f$ and $\tau_i$ and substituting the expressions obtained into Equations 4–6, we finally obtain

$$\frac{d^2 u_f}{dz^2} = \frac{C_f}{A_f E_f}(u_f - u_i) \quad (25a)$$

$$\frac{d^2 u_i}{dz^2} = -\frac{C_f}{A_i E_i}(u_f - u_i) - \frac{C_m}{A_i E_i}(u_m - u_i) \quad (25b)$$

$$\frac{d^2 u_m}{dz^2} = \frac{C_m}{A_m E_m}(u_m - u_i) \quad (25c)$$

where $u_f \equiv u(z, \bar{r}_f)$, $u_i \equiv u(z, \bar{r}_i)$, $u_m \equiv u(z, \bar{r}_m)$ and

$$C_f = \frac{2\pi G_f G_i}{G_f \ln(\bar{r}_i/r_f) + G_i \ln(r_f/\bar{r}_f)} \quad (26a)$$

$$C_m = \frac{2\pi G_i G_m}{G_i \ln(\bar{r}_m/r_i) + G_m \ln(r_i/\bar{r}_i)} \quad (26b)$$

One can rewrite Equations 25 in terms of the variables $u = u_f - u_i$ and $v = u_m - u_i$ to obtain

$$\frac{d^2 u}{dz^2} = \gamma_{f,i} u + \frac{C_m}{A_i E_i} v \quad (27a)$$

$$\frac{d^2 v}{dz^2} = \frac{C_f}{A_i E_i} u + \gamma_{i,m} v \quad (27b)$$

where $\gamma_{f,i} = C_f[(1/A_f E_f) + (1/A_i E_i)]$ and $\gamma_{i,m} = C_m[(1/A_i E_i) + (1/A_m E_m)]$. Since $u_f(0) = u_i(0) = u_m(0) = 0$, Equations 27 have as solutions $u = A_1 \sinh(\nu_1 z) + A_2 \sinh(\nu_2 z)$ and $v = B_1 \sinh(\nu_1 z) + B_2 \sinh(\nu_2 z)$, with

$$\nu^4 - (\gamma_{f,i} + \gamma_{i,m})\nu^2 + \left\{\gamma_{f,i}\gamma_{i,m} - \frac{C_f C_m}{(A_i E_i)^2}\right) = 0 \quad (28a)$$

$$\nu_{1,2}^2 = \frac{1}{2}\left\{(\gamma_{i,f} + \gamma_{i,m}) \pm \left[(\gamma_{i,f} - \gamma_{i,m})^2 + 4\frac{C_f C_m}{(A_i E_i)^2}\right]^{1/2}\right\} \quad (28b)$$

Putting back the expressions for $u$ and $v$ into Equations 27, one finds that of the four constants $A_1$, $A_2$,

$B_1$ and $B_2$ only two are independent. We choose

$$B_1 = \frac{A_i E_i(\nu_1^2 - \gamma_{i,f})}{C_m} = \frac{C_f}{A_i E_i} \times \left(\frac{1}{\nu_1^2 - \gamma_{i,m}}\right) = \eta A_1 \quad (29a)$$

$$A_2 = \frac{C_m}{A_i E_i}\left(\frac{1}{\nu_2^2 - \gamma_{i,f}}\right) = \frac{A_i E_i}{C_f}(\nu_2^2 - \gamma_{i,m}) = \xi B_2 \quad (29b)$$

$A_1$ and $B_2$ are in turn determined by the following boundary conditions: $u_f'(-L/2) = u_f'(L/2) = \alpha$, $u_i'(-L/2) = u_i'(L/2) = \beta$ and $u_m'(-L/2) = u_m'(L/2) = \delta$. The prime denotes differentiation with respect to $z$. Consequently

$$u'(L/2) = \nu_1 A_1 \cosh(\nu_1 L/2) + \nu_2 \xi B_2 \cosh(\nu_2 L/2) = \alpha - \beta \quad (30a)$$

$$v'(L/2) = \eta\nu_1 A_1 \cosh(\nu_1 L/2) + \nu_2 B_2 \cosh(\nu_2 L/2) = \delta - \beta \quad (30b)$$

By Equation 3, $\alpha$, $\beta$ and $\gamma$ have to satisfy the relation

$$A_f E_f \alpha + A_i E_i \beta + A_m E_m \delta = A_o \sigma_{apl} \quad (31)$$

We therefore obtain expressions for $A_1$ and $B_2$ in terms of $\alpha$, $\beta$ and $\gamma$:

$$A_1 = \frac{\xi(\delta - \beta) - (\alpha - \beta)}{\nu_1(\eta\xi - 1)\cosh(\nu_1 L/2)} \quad (32a)$$

$$B_2 = \frac{\eta(\alpha - \beta) - (\delta - \beta)}{\nu_2(\eta\xi - 1)\cosh(\nu_2 L/2)} \quad (32b)$$

$\sigma_f(z) = E_f u_f'(z)$ is obtained by integrating Equation 25a and using the boundary conditions for $u_f$:

$$\sigma_f(z) = E_f\alpha - \frac{C_f}{A_f}\left[\frac{a_1}{\nu_1}f_1(z) + \frac{\xi b_2}{\nu_2}f_2(z)\right] \quad (33)$$

where $a_1 = A_1\cosh(\nu_1 L/2)$, $b_2 = B_2\cosh(\nu_2 L/2)$ and $f_n(z) = 1 - \cosh(\nu_n z)/\cosh(\nu_n L/2)$, $n = 1, 2$. We go through a similar procedure for $\sigma_i$ and $\sigma_m$:

$$\sigma_i(z) = E_i\beta + \frac{C_f}{A_i}\left[\frac{a_1}{\nu_1}f_1(z) + \frac{\xi b_2}{\nu_2}f_2(z)\right] + \frac{C_m}{A_i}\left[\frac{\eta a_1}{\nu_1}f_1(z) + \frac{b_2}{\nu_2}f_2(z)\right] \quad (34)$$

$$\sigma_m(z) = E_m\delta - \frac{C_m}{A_m}\left[\frac{\eta a_1}{\nu_1}f_1(z) + \frac{b_2}{\nu_2}f_2(z)\right] \quad (35)$$

One can verify that

$$\lim_{L\to\infty}\frac{\sigma_f(0)}{E_f} = \lim_{L\to\infty}\frac{\sigma_i(0)}{E_i} = \lim_{L\to\infty}\frac{\sigma_m(0)}{E_m} = \frac{A_o\sigma_{apl}}{A_f E_f + A_i E_i + A_m E_m}$$

as it should in the limit of an infinite fibre provided that $E_f A_f\alpha + E_i A_i\beta + E_m A_m\delta = A_o\sigma_{apl}$. We finally give the expressions for the shear stresses $\tau_f$ and $\tau_i$:

$$\tau_f(z) = -\frac{C_f}{2\pi r_f}\left(a_1\frac{\sinh(\nu_1 z)}{\cosh(\nu_1 L/2)} + \xi b_2\frac{\sinh(\nu_2 z)}{\cosh(\nu_2 L/2)}\right) \quad (36a)$$

$$\tau_i(z) = \frac{C_m}{2\pi r_i}\left(\eta a_1\frac{\sinh(\nu_1 z)}{\cosh(\nu_1 L/2)} + b_2\frac{\sinh(\nu_2 z)}{\cosh(\nu_2 L/2)}\right) \quad (36b)$$

Note that the matrix region can be further divided into smaller regions. This "layering" process provides a radial dependence for the tensile stress in the matrix and obviously, an increasingly large number of layers considered in the theoretical equations is expected to yield results in closer agreement with real systems, i.e. in our case the computer model. In the case of $N$ regions considered (a fibre plus the interphase and $N$-2 matrix layers), Equation 27a for $\nu$ becomes a polynomial of order $2(N-1)$. The tensile and shear stresses in each of these regions are now expressed in the following form:

$$\sigma_m(z) = \alpha_m + \sum_{j=1}^{N-1} A_j\left(1 - \frac{\cosh(\nu_j z)}{\cosh(\nu_j L/2)}\right) \quad (37a)$$

$$\tau_m(z) = \sum_{j=1}^{N-1} B_j\frac{\sinh(\nu_j z)}{\cosh(\nu_j L/2)} \quad (37b)$$

where the subscript $j$ labels the different regions/phases and $N$ is the total number of regions/phases. $A_j$ and $B_j$ are amplitudes, functions of $C_j$ (for example, Equations 26 are for the case $N = 3$), $E_j A_j$, $\nu_j$ and the boundary condition $\alpha_j$ values (i.e. the values of $\sigma_j$ at $z = \pm L/2$).

In order to show the net improvement of our theoretical calculation as the number of layers $N$ is increased over the original shear-lag theory, we compare the tensile stress profile in the fibre and the shear stress profile at the fibre–interphase surface for a perfect interphase ($E_i = E_m$) as obtained from Cox shear-lag theory, and as obtained from the theory described above for $N = 3$ and $N = 4$ layers, with the results of the computer model taken from previous work [42]. Since we are comparing Cox shear-lag theory and our theory with the two-dimensional computer results, both Cox theory and our theory have been adapted to a two-dimensional geometry. Fig. 2 displays, as an example of how the various $r$ and $\bar{r}$ parameters are chosen, a fibre of length $L = 5$ (square sites), surrounded by a perfect interphase (circled sites), the remaining sites (dots) representing the matrix. According to Fig. 2, $\bar{r}_f = 0$, $\bar{r}_i = a_0^y$ and in the case $N = 4$, $\bar{r}_m = 2a_0^y$ where $a_0^y = 3^{1/2}a_0^x/2$, a unit length in the $y$ direction and $a_0^x$ is a unit length in the $x$ direction and $a_0^x \equiv 1$. However, choosing the values for $r_f$, $r_i$, $r_m$ and $r_{av}$ is not so obvious due to the discrete nature of the model. We choose to use the mid-point between the $\bar{r}$ values, i.e. $r_f = 0.5a_0^y$, $r_i = 1.5a_0^y$, ($r_m = 2.5a_0^y$ for the case $N = 4$) and $r_{av} = 24.5a_0^y$. $\bar{r}_{av}$ is taken to be the mid-point between $r_i$ and $r_{av}$ for $N = 3$, i.e. $\bar{r}_{av} = 13$, and the midpoint between $r_m$ and $r_{av}$ for $N = 4$, i.e. $\bar{r}_{av} = 13.5$.

We first consider two systems: one with a fibre–matrix modulus ratio $E_f/E_m = 4.4$, while both the interface and the matrix have the same elastic modulus $E_i = E_m$, and one with a fibre–matrix modulus ratio $E_f/E_m = 31.1$ also with $E_i = E_m$. Fig. 3a and b display the tensile stress profile along the fibre for a fibre length $L = 40$ (comparable to the critical length $l_c$ found for ratios $E_f/E_m = 4.4$ and 31.1 [42]) as obtained from the computer model at the point of failure, Cox shear-lag theory, and the present theory with $N = 3$ and $N = 4$. Fig. 3a is for $E_f/E_m = 4.4$ while Fig. 3b is for $E_f/E_m = 31.1$. Fig. 3c and d display the shear stress at the fibre–interphase surface for a fibre length $L = 40$. Fig. 4a and b show the tensile stress along the fibre while Fig. 4c and d show the tensile stress at the fibre–interphase surface as described above for Fig. 3 except that the fibre length is now $L = 120 \simeq 3l_c$.

Fig. 3 shows clearly the discrepancies between the results of Cox shear-lag theory and the computer model, as well as the improvement of our calculation over Cox shear-lag theory. We compare the results from the model and both theoretical calculations using three criteria: the value of the tensile stress at the fibre mid-point ($z = 0$), the value of the shear stress at the fibre end-points ($z = \pm L/2$) and the shape of the tensile curve. A significant discrepancy in the value of the shear stress at the fibre end-points exists between Cox shear-lag theory and the computer model. This results in a considerable discrepancy in the shape of the tensile stress curve (see Fig. 3a and b). A discrepancy in the shape of the tensile stress, i.e. its degree of "flatness", can lead to incorrect estimates of the percentage of the fibre length carrying a stress close to the maximum fibre stress $\sigma_f(z = 0)$. For instance, according to Fig. 3a one estimates this percentage to be approximately 10% for Cox shear-lag theory while it is approximately 50% in the computer model. The differences between Cox shear-lag theory and the computer model increase as the elastic modulus ratio $E_f/E_m$ increases (see Fig. 3b and d); this is consistent with the fact that Cox's assumption of a constant tensile stress in the matrix $\sigma_m(z, r) \equiv \sigma_{apl}$ becomes worse as $E_f/E_m$ increases.

In contrast to Cox's theory, our calculation shows much better agreement. Our results for the amplitude of the shear stress at the fibre ends and for the overall shape of the tensile stress profile are in very close agreement with the computer model results. As one may notice in Fig. 3a and b, our theoretical calculations for the tensile stress profile seem to converge to values slightly higher than those of the computer model. Also, the theoretical stress profiles calculated from our model in the case of the short fibre ($L = 40$) are slightly higher compared to the case of the long fibre ($L = 120$) (compare Fig. 3a with Fig. 4a and Fig. 3b with Fig. 4b). These effects can be attributed to the fact that the ratio of the fibre length to the linear dimension $L_x$ of the system was kept constant, hence the system used was proportionally smaller in the case of the shorter fibre ($L = 40$). The discreteness of our model introduces rather sharp variations in the stress amplification pattern at the fibre tips, especially when small systems are used. We then proceeded to input the value of the tensile stress at the fibre tips obtained from the simulation model into our equations as boundary conditions, and this explains why the theoretical stress profiles obtained are slightly higher than they should be in the case of the shorter fibre, and the excellent agreement between the simulation model and our calculation in Fig. 3a is probably fortuitous. Finally, the increased discrepancy between Cox's shear-lag theory and the computer model results for $E_f/E_m = 31.1$ suggests that a greater number of layers $N$ need to be considered in our theoretical description as the elastic modulus ratio $E_f/E_m$ increases.

As the fibre length $L$ increases (see Fig. 4) the function $f = 1 - \cosh(\beta z)/\cosh(\beta L/2)$ in Cox's expression for the fibre tensile stress in Equation 11 becomes length-insensitive for $L$ such that for $\beta L/r_f > 5$, $f \approx 1$ and the value of the stress at the fibre mid-point simply tends towards the value of the stress of an infinite fibre $E_f\varepsilon^*$. Here $\varepsilon^*$ is the composite strain at failure. Fig. 4c and d still show a significant discrepancy between the amplitude of the shear stress at the fibre end-points from Cox shear-lag theory and the model, as well as the net improvement of our expression for the shear stresses for $N = 3$ and $N = 4$ layers compared with Cox shear-lag theory. However, the above-mentioned discrepancy in Cox shear-lag theory leads in this case to a lesser difference in the shape of the tensile stress in Fig. 4a and b (compare with Fig. 3a and b) in the sense that the regions of discrepancy (usually close to the fibre ends) represent a decreasing percentage of the total fibre length $L$ as $L$ increases. Another interesting fact to note is that the discrepancy between the maximum shear stress at the fibre end-points $\tau_f(z = \pm L/2)$ from Cox shear-lag theory and the computer model (a factor of 2.8 in Fig. 3c, and of 3.1 in Fig. 3d) is consistent with the experimentally determined factor of at least 2 cited in the literature [43].

Our theoretical analysis indicates that the poor agreement of Cox and Dow shear-lag theory [31, 43, 44] with experimental measurements of shear stresses does not seem to be due to the "no-load" boundary condition at the fibre ends $\sigma_f(z = \pm L/2) = 0$. In fact the "no-load" boundary condition is justified in the case of chopped fibres, where there is no end-face adhesion, and should be good enough in the case of

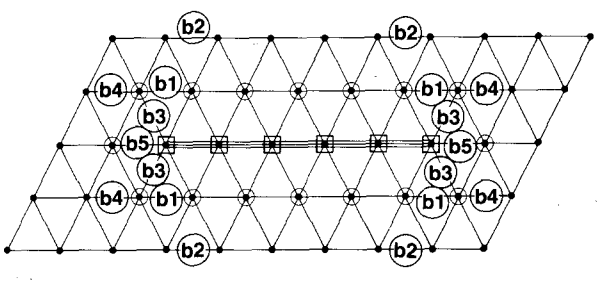


*Figure 2* Example of (⊡) a fibre of length $L = 5$, surrounded by (⊙) a perfect interphase and (●) the matrix sites immediately next to the interphase, on a triangular lattice. b1–b5 illustrate the location of various bonds which we will refer to in the text. b1 is an interphase tensile bond, b2 is a matrix tensile bond, b3 is an interphase shear bond, b4 is a matrix tensile bond next to the interphase bond b1 and b5 is an interphase tensile bond next to the fibre end.

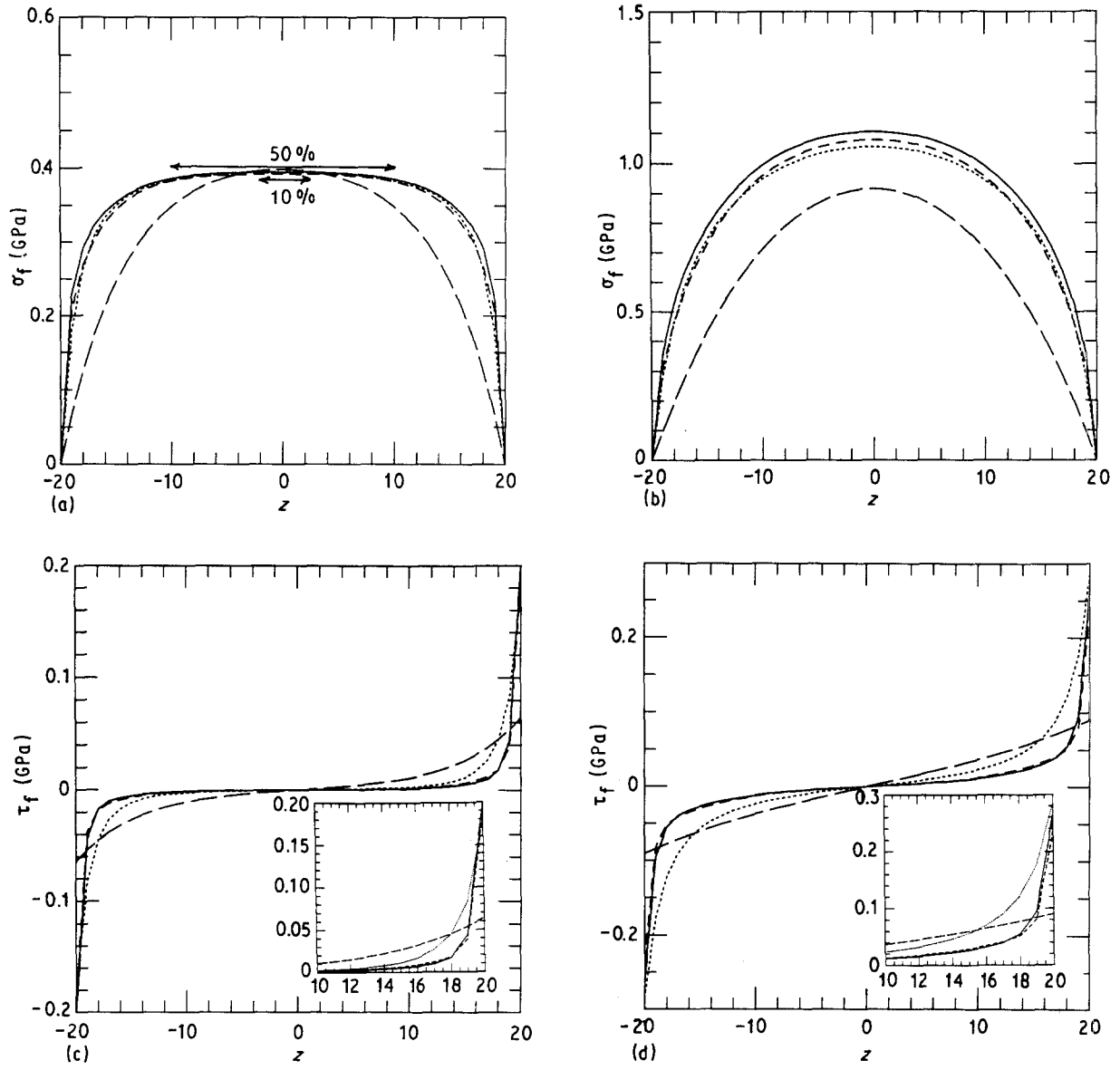


*Figure 3* (a) Tensile stress profile for a fibre–matrix modulus ratio $E_f/E_m = 4.4$ and length $L = 40 \simeq l_c$. The $y$ axis represents the fibre tensile stress ($\sigma_f$), while the $x$ axis represents the distance $z$ along the fibre with the origin at the fibre mid-point and is in units of the lattice constant $a_0$ which is arbitrarily set to unity. (— —) Cox's prediction [25], (– – –) $N = 3$ layer model, (——) $N = 4$ layer model, (· · ·) computer model. The arrows represents the fraction of the fibre length carrying a stress close to the fibre maximum stress for Cox's calculation (10%) and for the $N = 3$ and $N = 4$ layer model calculation (50%). (b) Same as for (a) but for a fibre–matrix modulus ratio $E_f/E_m = 31.1$. (c) Shear stress profile along the fibre–interphase surface for a fibre–matrix modulus ratio $E_f/E_m = 4.4$. The $y$ axis represents the shear stress ($\tau_f$), while the $x$ axis represents the distance $z$ along the fibre (see Fig. 3a). The insert amplifies the region between $z = 10$ and $z = 20$. (d) Same as (c) for a fibre–matrix modulus ratio $E_f/E_m = 31.1$.

whiskers. One can imagine that in the limit of a thin fibre, the contribution to the load transfer from the tensile stress acting on the fibre end-faces becomes negligible compared to the contribution from the shear stresses acting along the fibre surface as the fibre cross-sectional area is vanishing. The discrepancy is rather due to the fact that the matrix tensile stress does not have any radial dependence $\sigma_m(z, r) = \sigma_m(z)$ (Dow) or is assumed constant $\sigma_m(z, r) = \sigma_{apl}$(Cox). In fact, the assumptions of Cox and Dow are equivalent, since computer model results show that the tensile stress in the matrix around the fibre possesses a very weak axial dependence (if one discards the stress amplification effects at the fibre end-points, of course) but a significant radial dependence which is neglected by both theories. We therefore conclude that Cox shear-lag theory is unable to properly describe the tensile and shear stress profiles in the case of a single short fibre embedded in a matrix. However, the prediction of Cox shear-lag theory for the tensile stress profile of the fibre is expected to be satisfactory in the limit of low elastic modulus mismatch, or in the limit of very long fibres (typically several times longer than their critical length) so the regions of discrepancy become negligible.

At this point, the obvious thing to do is to increase the number of layers for increasingly better results. One soon runs into the following problem, which is the main drawback of our theoretical development: the precise knowledge of the boundary conditions $\alpha_j (j = 1, N)$ as the number of layers $N$ in the matrix increases. In order to generate the stress profiles presented in Figs 3 and 4, the required boundary conditions were taken from the computer model, i.e. the

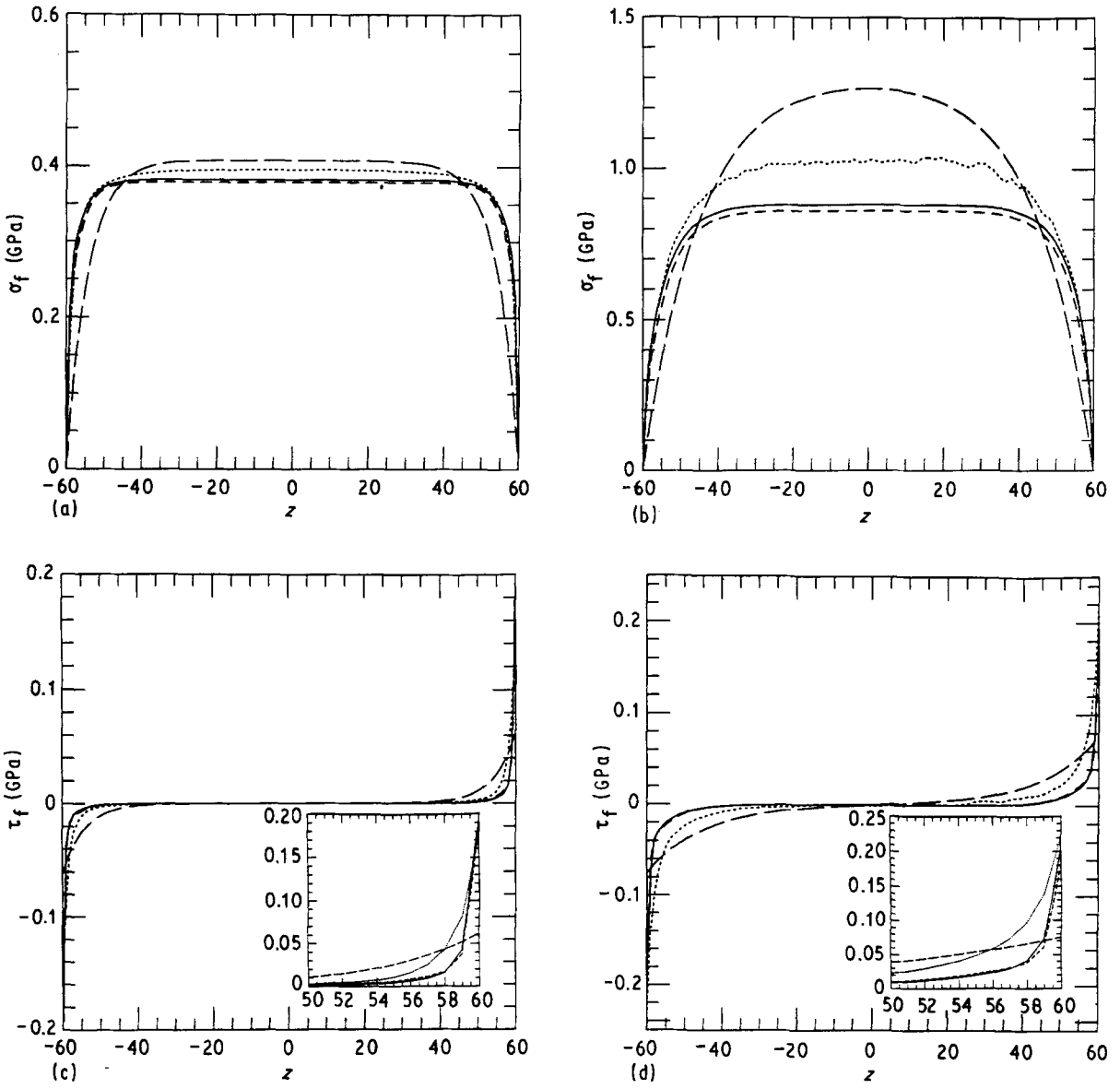


*Figure 4* (a) Tensile stress profile along the fibre for a fibre–matrix modulus ratio $E_f/E_m = 4.4$ and length $L = 120 \simeq 3l_c$ (see Fig. 3a). (b) Same as (a) but for a fibre–matrix modulus ratio $E_f/E_m = 31.1$. (c) Shear stress profile along the fibre–interphase interface for a fibre–matrix modulus ratio $E_f/E_m = 4.4$ and length $L = 120$ (see Fig. 3c above). The insert amplifies the region between $z = 50$ and $z = 60$. (d) Same as (c) for a fibre–matrix modulus ratio $E_f/E_m = 31.1$.

values of $\sigma_i(z = \pm L/2)$ for $N = 3$ and $N = 4$, plus $\sigma_m(z = \pm L/2)$ for $N = 4$; $\sigma_{av}$ was simply taken to be equal to $E_m\varepsilon^*$. Thus our theoretical derivation may be of phenomenological interest, but it is of little practical use. Considering the fact that these boundary conditions cannot be obtained from first principles, and that we were able to obtain such good agreement between the computer model and our theoretical development, we feel confident to resort only to the computer model to study the effect of interphase elastic modulus and cohesive energy on the critical aspect ratio. We will present in section 3 the results from our computer model.

## 3. Model and computer results

The model [42] is a coarse-grained spring model on a two-dimensional triangular grid. The Hamiltonian features a two-body as well as a three-body term:

$$H = \frac{1}{2}\sum_{ij} E_{ij}(r_{ij} - r_0)^2 + \frac{1}{2} \times \sum_{ijk} c_{ijk}(\cos\theta_{ijk} - \cos\theta_0)^2 \qquad (38)$$

where $r_0 = 1$ is the equilibrium bond length and $\theta_0 = \pi/3$ is the equilibrium angle between bonds for a triangular lattice. $E_{ij}$ is equal to $E_f$ if the nodes $i$ and $j$ are both fibre nodes, to $E_i$ if the nodes $i$ and $j$ are either both interphase nodes or one fibre and one interphase node, and to $E_m$ if the nodes $i$ and $j$ are either both matrix nodes or one matrix and one interphase node. The constants $c_{ijk} = c_f$ if bonds $ij$ and $jk$ are fibre bonds, to $c_i$ if bonds $ij$ and $jk$ are both interphase bonds or one fibre and one interphase bond, respectively, and to $c_m$ if bonds $ij$ and $jk$ are both matrix bonds or one matrix and one interphase bond,

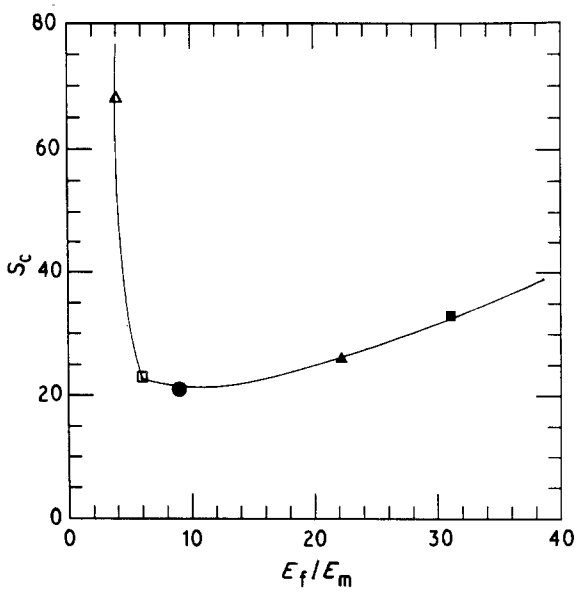


*Figure 5* Critical aspect ratio $S_c$ as a function of the fibre–matrix modulus ratio $E_f/E_m$ = (△) 4, (□) 6, (●) 9, (▲) 22.2 and (■) 31.1. The $y$ axis is in units of $1/d_f^w = 14.9/a_0^x$, where $a_0^x$ is a unit length in the $x$ direction. The line does not represent a fit to the data.

respectively. The constants $c_{ijk}$ ensure that the fibre, the interphase and the matrix each have their own Poisson ratio. A triangular lattice possesses the following Poission ratio:

$$\nu_\alpha = \frac{E_\alpha - 9(c_\alpha/2r_0^2)}{3E_\alpha + 9(c_\alpha/2r_0^2)} \tag{39}$$

and shear modulus

$$G_\alpha = \frac{\sqrt{3}}{4}\left(E_\alpha + \frac{9c_\alpha}{2r_0^2}\right) \tag{40}$$

where $\alpha$ = f, i or m. The interphase is given a Poisson ratio equal to the matrix Poisson ratio $\nu_i = \nu_m = 0.1$, corresponding to the following values for the $c$-constants $c_m = E_m/7$ and $c_i = E_i/7$, which ensures that the Poisson ratio of the interphase or the matrix does not vary with its respective elastic modulus. Polymer matrices have a Poisson ratio around 0.3 while glass has a Poisson ratio around 0.2. Since the fibre considered in this work is unidimensional, i.e. it consists of a single line of nodes, we assumed [42] that it has a null Poisson ratio. The matrix material was therefore given a Poisson ratio of 0.1 in order to achieve the same relative Poisson ratio $\nu_m - \nu_f$ found in a real system (i.e. glass–epoxy). However, it will be shown later that this unidimensional fibre might have an effective diameter $d_f^w$ of $a_0^x/14.9$, and that unidimensional fibre probably has a Poisson ratio closer to one-third than zero. Periodic boundary conditions are applied in the direction of applied tensile strain (the $x$ axis), while free boundary conditions are applied in the $y$ direction. The system is relaxed to its minimal energy configuration upon application of a uniform strain with the help of a conjugate gradient technique [42]. The model incorporates a fracture criterion via the cohesive energy parameters, in which a bond is broken if it accumulates an energy equal to or greater than its assigned cohesive energy $U_f$ for a fibre bond, $U_i$ for an interphase bond and $U_m$ for a matrix bond.

The critical length is defined to be the length at which fracture is initiated in the matrix (or the interphase region) and at the middle of the fibre simultaneously. The "no-load" boundary conditions $\sigma_f(z = \pm L/2)$ have been used in all theoretical calculations since in the computer model, the fibre always debonds at the ends before catastrophic failure occurs (bonds b5 in Fig. 2 break). A detailed explanation of how the critical length is measured is given elsewhere [42]. Fracture in the interphase or in the matrix can occur via two modes: the breaking of a bond carrying tensile stress (tensile mode) or the breaking of a bond carrying shear stress (shear mode). The first part of this section will show computer data concerning the influence of interphase elastic moduli on the measured critical aspect ratio, and will discuss the various modes of failure encountered. The second part will show computer data concerning the influence of interphase cohesive energy on the critical aspect ratio.

## 3.1. Interphase elastic modulus

Fig. 5 displays a plot of critical aspect ratio $S_c = l_c/d_f$ versus $E_f/E_m$ for $U_f/U_m = 2$ for a perfect interphase $E_i = E_m$ and $U_i = U_m$, where $d_f$ is the fibre diameter. Fig. 5 is taken from our earlier paper [42]. We point out the two divergences in the critical aspect ratio, one at low values of $E_f/E_m$, and the other for large values of $E_f/E_m$, as well as the minimum critical aspect ratio at a value of $E_f/E_m$ between 8 and 14. We refer to the value of $E_f/E_m$ at the location of a minimum in the critical aspect ratio as the "optimum fibre–matrix modulus ratio" (OFMR). The divergence to the left of the OFMR, theoretically determined to be at $E_f/E_m = U_f/U_m$, is explained by the fact that for a perfect elastic–brittle system, it is impossible to obtain simultaneous failure of the matrix and fibre for a finite fibre length if $E_f/E_m \leq U_f/U_m$. The divergence to the right of the OFMR is due to the fact that the fibre failure stress $\sigma_f^* = (2E_fU_f)^{1/2}$ increases as $E_f$ increases, as well as the shear stresses generated at the fibre tips, hence one needs increasingly longer fibres in order to obtain simultaneous failure of the fibre and the matrix. Fibres whose aspect ratio is above the critical aspect ratio line in Fig. 5 are supercritical, and break well before the matrix, while fibres whose aspect ratio is below the critical aspect ratio line are subcritical, in which case the matrix fails well before the fibre.

The five symbols in Fig. 5 represent the five systems selected in our study of the influence of interphase modulus on the critical aspect ratio, namely $E_f/E_m = 4$ (open triangle), 6 (open square) 9 (full circle), 22.2 (full triangle) and 31.1 (full square). The cohesive energy parameters have been chosen as above: $U_f = 2U_m$ and $U_i = U_m$. Fig. 6 illustrates the resulting critical aspect ratio dependence for the five chosen systems. All curves possess the same qualitative shape as in Fig. 5: divergence at both low and high values of the elastic modulus ratio $E_f/E_i$ as well as a minimum critical aspect ratio at a given value of

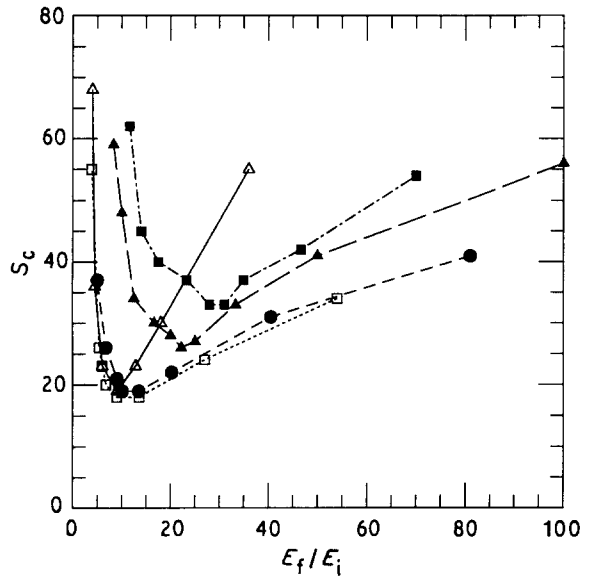


*Figure 6* Critical aspect ratio $S_c$ as a function of fibre–interphase modulus ratio $E_f/E_i$ = (△, ——) 4, (□, ···) 6, (●, – – –) 9, (▲, — —) 22.2 and (■, —·—) 31.1. The $y$ axis is in units of $1/d_f^w = 14.9/a_0^x$, where $a_0^x$ is a unit length in the $x$ direction. The lines do not represent a fit, but are added to help visualize the data.

$E_f/E_i$, the "optimum fibre–interphase modulus ratio" (OFIR). For $E_f/E_m = 4$ the OFIR is roughly 9, consistent with the OFMR for the single fibre with a perfect interphase shown in Fig. 5. The value of $E_i$ at the OFIR moves towards $E_m$ as the fibre elastic modulus increases. For the cases $E_f/E_m = 6$ and 9, the OFIR is between 9 and 13.5 for the former and between 10 and 13.5 for the latter. Those values are consistent with the location of the OFMR in Fig. 5. As the fibre becomes increasingly stiff, the OFIR remains at $E_i = E_m$ due to large stress amplification in the matrix for $E_i > E_m$ (this will be explained in more detail below). The divergence in the critical aspect ratio to the right of the OFIR in all five curves of Fig. 6 can be understood as follows: as $E_i$ decreases, the load transfer between the matrix and the fibre is compromised, i.e. the interphase accommodates the applied strain, and the fibre sees very little strain (or equivalently stress) transferred. On the other hand, the divergence in the critical aspect ratio to the left of the OFIR is due to the strain/stress amplification in the matrix bonds caused by the stiffer interphase ($E_i > E_m$) and the fibre, such that one needs an increasingly longer fibre to ensure simultaneous failure of the fibre and the matrix. In fact, for high-modulus fibres, a stiff interphase $E_i > E_m$ always increases load transfer, but embrittles the composite material: the strain at failure is much less than for the case $E_i = E_m$. This accounts for the fact that minimum critical aspect ratio in Fig. 6 remains at $E_i = E_m$ for the systems with $E_f/E_m = 22.2$ or 31.1.

Fig. 7a illustrates the tensile stress along the fibre for a system with a fibre–matrix modulus ratio of 31.1 and a fibre length $L = 32$ (close to the critical length for $E_i = E_m$) at a constant applied strain of 1.44%. The fibre–matrix cohesive energy ratio $U_f/U_m$ remains equal to 2. In this particular case, no bonds other than the end bonds b5 are allowed to break. The perfect interphase ($E_i = E_m$, short dashed line) is compared to a stiffer interphase ($E_i = 2E_m$, dotted line): for the same applied strain, the load transfer to the fibre is slightly better for the stiffer interphase. The solid line represents the fibre failure stress $\sigma_f^* = (2E_f U_f)^{1/2}$. Fig. 7b is a plot of the energy stored in the bonds along the row of nodes above the fibre (all interphase tensile bonds between the two b4 bonds in Fig. 2, including the matrix bonds b4 themselves). The short dashed line represents $E_i = E_m$ while the dotted line represents $E_i = 2E_m$, and the horizontal solid line represents the matrix and the interphase failure threshold $U_i = U_m$. The energy stored in bond b4 (located at $z = \pm 17$) is close to failure for the case of the perfect interphase, while it is well above failure for the case of the stiffer interphase. If the bonds had been allowed to break, bond b4 would have failed at a much lower value of the applied strain, $\sigma_{apl} \simeq 1.3\%$, decreasing the

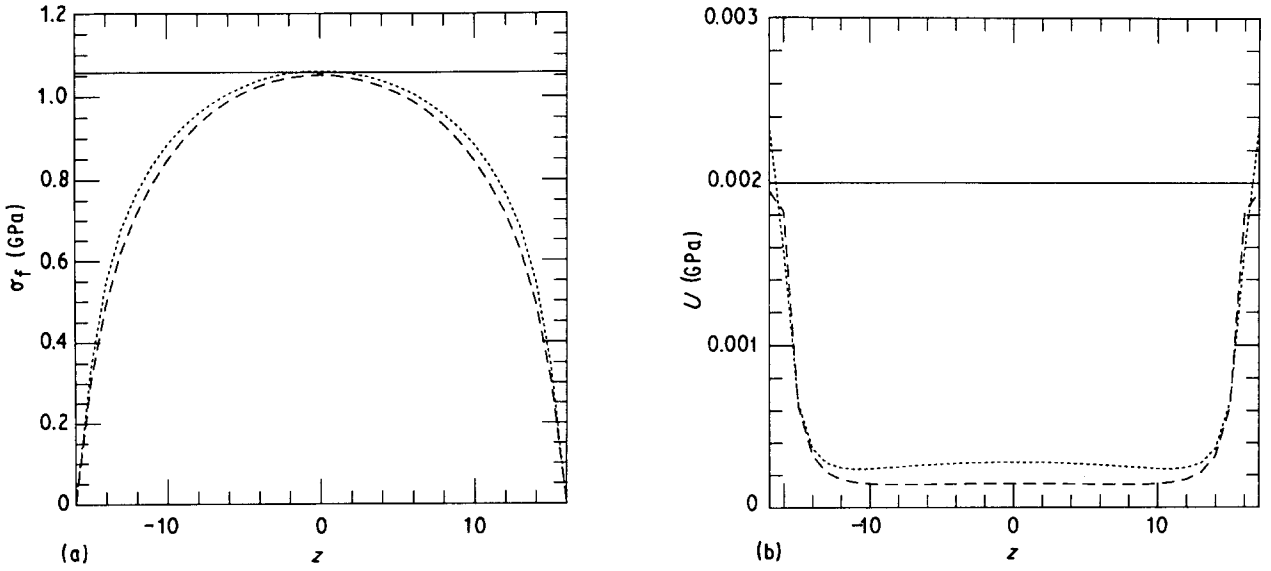


*Figure 7* (a) Tensile stress profile along the fibre (same as Fig. 3a) for a system with $E_f/E_m = 31.1$ and $U_f/U_m = 2$, fibre length $L = 32$ at an applied strain $\varepsilon_{apl} = 1.44\%$, for (– – –) $E_i = E_m$ and (···) $2E_m$; (——) fibre failure threshold. (b) Plot of the energy $U$ as a function of $z$ (see Fig. 3a) stored in the tensile bonds along the row of nodes above the fibre for (– – –) $E_i = E_m$ and (···) $2E_m$; (——) matrix and interphase failure threshold $U_i = U_m$.

amount of stress transferred to the fibre at the failure point. One needs a longer fibre in order to achieve simultaneous failure of the fibre mid-point and the matrix bond b4, hence the critical length increases for $E_i > E_m$. The results of Fig. 7a and b suggest that a study of load transfer should not be dissociated from a failure criterion because the fibre stress level itself is of limited utility. Also note that as $E_i$ tends towards $E_f$, we are simply dealing with a thicker fibre (in Fig. 2 that thicker fibre would include the original five fibre nodes plus the circled nodes on the rows immediately above and below the fibre nodes; hence the fibre has a diameter $d_f = 2a_0^y = \sqrt{3}a_0^x$). Hence, as $E_f/E_i \to 1$, the new fibre has a diameter several times greater than the original fibre diameter and one should therefore expect a fast divergence in Fig. 6 as $E_f/E_i \to 1$.

It is difficult to give an estimate of the unidimensional fibre diameter (other than using the area per bond which yields $d_f^w = a_0^x/2\sqrt{3}$), since the model used is coarse-grained, i.e. information concerning phenomena occurring at length scales less than a certain cutoff length is lost. At that particular length scale, a fibre with an otherwise well-defined diameter may appear to be unidimensional. We expect the unidimensional fibre diameter to be roughly an order of magnitude smaller than the thicker fibre diameter $d_f/d_f^w \sim 10$. We attempt to estimate $d_f/d_f^w$ with the help of Fig. 8, which is a plot of the inverse fibre diameter $1/d_f^w$, where w represents the unidimensional fibre, as a function of $E_f/E_m$. The solid line represents the inverse fibre diameter as determined by the average of the data, $1/d_f^w = 14.9/a_0^x$. The error bars come from the discrete nature of the simulation model, where critical lengths are determined up to a precision of one lattice constant. The inverse fibre diameter is obtained from the assumption of constant aspect ratio, i.e. $l_c^w/d_f^w = l_c/d_f$, where $l_c/d_f$ is the critical aspect ratio taken from our earlier work [42] for a fibre of diameter $d_f = 2a_0^y = 3^{1/2}a_0^x$. A Poisson ratio close to 0.3 was chosen for the thick fibre, and this means that the

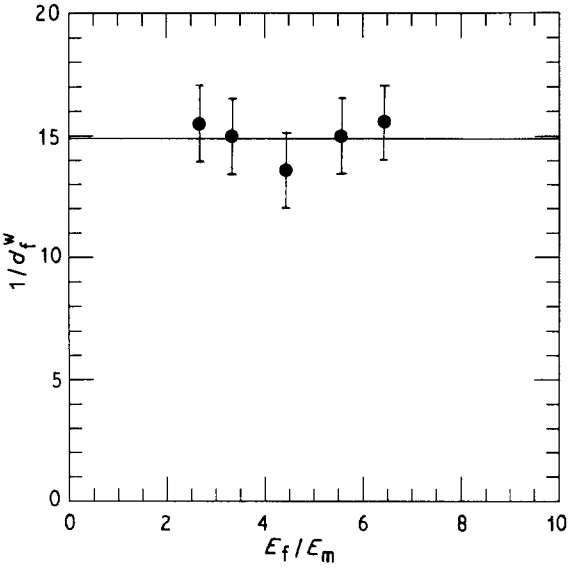


*Figure 8* Plot of the inverse whisker-like fibre diameter $1/d_f^w$ as a function of $E_f/E_m$. The horizontal line traced through the data represents the average inverse fibre diameter. The error bars are due to the discrete nature of the lattice: critical lengths are measured with a precision of $\pm$ 1 lattice constant.

constant $c_f$ ($\alpha \equiv f$) is small, i.e. $c_f \to 0$. In the limiting case $c_f = 0$, the fibre Poisson ratio is 1/3 from Equation 40 and the energy stored in the fibre bonds comes uniquely from the two-body term in the Hamiltonian (Equation 39). By selecting a constant $c_f$ close to zero, one ensures in this way that the main contribution to the fracture energy of the thick fibre is from the two-body term in Equation 39 which causes the tensile bond at the fibre mid-point to fail, so one might be justified to compare this fibre to the unidimensional fibre (i.e. using $l_c^w/d_f^w = l_c/d_f$), where 100% of the fracture energy is due to the two-body term in Equation 39. According to Fig. 8, the interphase diameter depicted in Fig. 2 is roughly $d_f/d_f^w = 14.9/a_0^x(3^{1/2}a_0^x) = 25$ times greater than the fibre diameter $d_f^w$. Using the expression for $d_f^w$ obtained from the area per bond, we obtain $d_f/d_f^w = 2\sqrt{3}/a_0^x \cdot \sqrt{3}a_0^x = 6$. We therefore estimate that the ratio of the interphase diameter to that of the unidimensional fibre probably lies in the range $6 < d_f/d_f^w < 25$. These figures represent a rough estimate only.

In order to understand how the interphase cohesive energy affects the overall properties of the composite, one needs to understand the various failure modes present. Before we proceed in the following section to study the influence of interphase cohesive energy, we identify the different modes of failure in the five selected systems. We refer the reader to the bonds as labelled in Fig. 2.

### 3.1.1. Systems with a fibre–matrix modulus ratio less than the OFMR

For $E_f/E_m = 4$, failure of composites to the right of the OFIR (OFIR $\simeq$ OFMR) is initiated in the matrix bond b2 carrying tensile stress. To the left and around the OFIR, failure is initiated in the interphase bond b1 carrying tensile stress. This is to be expected, since the load transfer is not very efficient in composites with a low value of $E_f/E_m$. Consequently, large tensile stresses remain for the matrix to bear (note that the energy depends on the second power of the stress), especially at low values of the interphase modulus $E_i$, where stress transfer is even worse. By lowering the interphase modulus $E_i$, one is in fact decreasing the amount of coupling between the matrix and the fibre. In the limit $E_i \to 0$, matrix and fibre are completely decoupled. As $E_i$ increases, the load transfer becomes more efficient. More stress is therefore shifted from the matrix to both the fibre and the interphase as matrix and fibre are more strongly coupled, and the location of failure moves from the matrix tensile bond b2 to the interphase tensile bond b1 (Fig. 9a).

### 3.1.2. Systems with a fibre–matrix modulus ratio in the vicinity of the OFMR

For $E_f/E_m = 6$, failure of composites to the right of the OFIR ($13.5 < E_f/E_i < 54$) is initiated in the interphase bond b3 carrying shear stress. The failure of composites with $E_f/E_i$ around the OFIR ($9 \leq E_f/E_i \leq 13.5$, and consistent with the location of the OFMR in Fig. 5) is initiated in the interphase bond b1 carry-

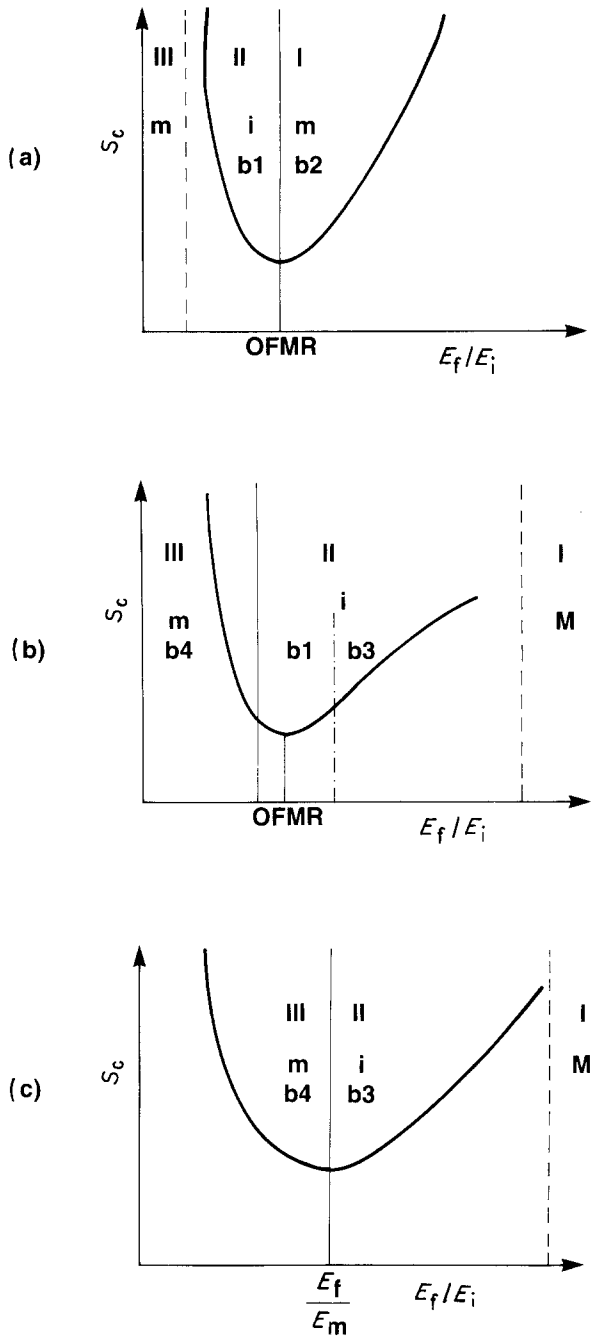


*Figure 9* Sketch of failure regions as a function of the fibre–interphase modulus ratio $E_f/E_i$. (a) The curve illustrates the critical aspect ratio for a low fibre–matrix modulus ratio. The solid vertical line at $E_f/E_i$ = OFMR represents the boundary between region II (interphase failure, initiated in bond b1 of Fig. 2) and region I (matrix failure, initiated in bond b2). The vertical dashed line represents the boundary between region II and region III. The exact location of this boundary is not known since region III is hypothesized in the limit $E_f/E_i \to 1$. (b) The solid curve illustrates the critical aspect ratio for a fibre–matrix modulus ratio close to the OFMR. The solid vertical line at $E_f/E_i <$ OFMR represents the boundary between region III (matrix failure initiated in bond b4 of Fig. 2) and region II (interphase failure initiated in bond b1). The vertical dot-dashed line located at $E_f/E_i >$ OFMR within region II represents the boundary between failure initiated in the interphase bond b1 and failure initiated in the interphase bond b3. The vertical dashed line represents the boundary between region II and region I. The exact location of this boundary is not exactly known, since region I is hypothesized in the limit $E_f/E_i \to \infty$. (c) The solid curve illustrates the critical aspect ratio for a high fibre–matrix modulus ratio. The solid vertical line located at $E_f/E_i = E_f/E_m$ represents the boundary between region III (matrix failure initiated in bond b4) and region II (interphase failure initiated in bond b3). The vertical dashed line represents the boundary between region II and region I. This boundary is not well defined for the same reason as in (b).

ing tensile stress, and to the left to the OFIR ($E_f/E_i < 9$) in the matrix bond b4 carrying tensile stress.

For $E_f/E_m = 9$, failure of composites to the right of the OFIR ($13.5 < E_f/E_i < 81$) (note that the upper bond on $E_f/E_i$ is greater than in the preceding case) is initiated again in the interphase bond b3 carrying shear stress. Failure of composites with $E_f/E_i$ around the OFIR ($10 < E_f/E_i \leq 13.5$, and consistent with the location of the OFMR in Fig. 5) is initiated in the interphase bond b1 carrying tensile stress, and failure of composites to the left of the OFIR ($E_f/E_i \leq 10$) is initiated in the matrix bond b4 carrying a tensile stress.

The failure mechanisms for $E_f/E_m = 6$ and 9 are very similar (Fig. 9b). The stress transfer is better as $E_f$ increases, which implies that a smaller level of tensile stress is left for the matrix to carry. The locus of failure consequently shifts from the matrix (bond b2) to the interphase region (either bond b3 or b1), unless $E_i$ is extremely compliant. One can imagine the case in which the interphase elastic modulus $E_i$ is sufficiently compliant ($E_i \to 0$) such that fibre and matrix are almost totally decoupled. The efficiency of load transfer is reduced to such an extent that the locus of failure is expected to be pushed back into the matrix (region I in Fig. 9b). The simulation results show two different failure modes occurring inside the interphase region. At low values of $E_i$, the stiff fibre causes a large strain concentration in bond b3, in the sense that the more compliant interphase bonds accommodate the applied strain and as explained above, the matrix–fibre coupling is not optimal. However, the matrix does not carry such a large stress level compared to the previous case of a low fibre–matrix modulus ratio. Hence the interphase shear bond b3 always breaks before the matrix tensile bond b2.

The coupling between fibre and matrix tends towards optimal conditions as the interphase stiffens. As this coupling increases, the location of failure has to shift eventually from the interphase shear bond b3 to the matrix tensile bond b4. However, in the present case of a relatively compliant fibre ($6 \leq E_f/E_m \leq 9$), the failure location does not directly shift from bond b3 to bond b4. There exists a range of values for the interphase elastic modulus (here $9 \leq E_f/E_i \leq 13.5$) for which stress builds up more rapidly in the interphase tensile bond b1 than in the interphase shear bond b3 or the matrix tensile bond b4. Upon application of additional strain, bond b1 will accommodate a larger part of the strain compared to the bonds b4 and b3 for the following reason: the compliance of bond b1 is greater than the compliance of bond b4 and bond b1 is parallel to the load while bond b3 is not. Furthermore, at this stage the compliance of the interphase is supposedly low enough so that the fibre no longer causes strain amplification in the interphase shear bond b3. This "b1" mode of failure plays a role only in composites whose fibre–matrix modulus ratio is close to or equal to the OFMR (see Fig. 9b). As the modulus of the fibre increases further, failure is expected to shift directly from the interphase shear bond b3 to the matrix tensile bond b4 (Fig. 9c).

### 3.1.3. Large elastic modulus ratio

For $E_f/E_m = 22.2$, failure of composites with $E_i < E_m$ is initiated in the interphase bond b3 carrying shear stress while failure of composites with $E_i \geq E_m$ is initiated in the matrix bond b4 carrying tensile stress. As discussed above, the location of failure shifts directly from the interphase shear bond b3 to the matrix tensile bond b4 and no more failure is initiated in the interphase tensile bond b1 (see Fig. 9c).

For $E_f/E_m = 31.1$, failure of composites with $E_i \leq E_m$ is initiated in the interphase bond b3 carrying a shear stress while failure in composites with $E_i > E_m$ is initiated in the matrix bond b4 carrying tensile stress. The fibre is now stiff enough so that the strain amplification in bond b3 can only be reduced if $E_i = E_m$ (see Figs 7a and b). For $E_i > E_m$, failure is directly shifted from bond b3 to b4 (see Fig. 9c).

The results of Fig. 6 for the critical aspect ratio dependence on interphase modulus show that a substantial decrease in critical aspect ratio is achieved for the composites whose fibre–matrix modulus ratio is less than the OFMR in Fig. 5. A minimum critical aspect ratio is found for a fibre–interphase modulus ratio close to or equal to the OFMR itself (compare the minimum critical aspect ratio found in Fig. 6 with the results for the perfect interphase $E_i = E_m$ in Fig. 5). A similar decrease in the critical aspect ratio cannot be achieved for composites whose fibre–matrix modulus ratio is greater than the OFMR in Fig. 5, in which case the critical aspect ratio is minimum for the perfect interphase $E_f/E_i = E_f/E_m$.

The different modes of failures identified can be organized into three different regions as shown in Fig. 9. Fig. 9a is a sketch of the various failure modes encountered as $E_i$ is varied for a composite with a fibre–matrix modulus ratio much less than the OFMR (for instance, $E_f/E_m = 4$ and the OFMR is in the vicinity of 8 to 14 for $U_f/U_m = 2$). Failure for composites located in region I occurs in the matrix (bond b2) while failure in region II occurs in the interphase (bond b1). The boundary between regions I and II is located at $E_f/E_i \simeq$ OFMR. Region III should be encountered as the interphase modulus is increased, since we know that in the limit $E_i \to E_f$, we recover a thicker fibre with a perfect interphase and failure has to occur in the matrix. Fig. 9b sketches the failure modes for a composite whose fibre–matrix modulus ratio is close to, but not greater than the OFMR (in this case, $6 \leq E_f/E_m \leq 9$). We expect region I to recede as regions II and III are expanding to the right. Failure in region I would presumably occur in the matrix, for $E_i$ low enough; failure in region II occurs in the interphase (bonds b3 and b1) while failure in region III occurs in the matrix (bond b4). The boundary between regions I and II is not well defined, but the boundary between regions II and III is located at $E_f/E_i \leq$ OFMR, i.e. $E_f/E_i \simeq 6$. There is a transition in the location of failure inside the interphase itself: from shear bond b3, where $E_f/E_i >$ OFMR, to tensile bond b1, where $E_f/E_i \approx$ OFMR. In particular, this failure information can be important in the case where anisotropies are introduced in the interphase region. Fig. 9c sketches the failure modes for the composites with a fibre–matrix modulus ratio greater than the OFMR. Failure in region I occurs in the matrix. Region I is probably receding even further to the right. In region II, failure occurs in the interphase (bond b3), while in region III, failure occurs in the matrix (bond b4). There is no longer a failure transition from bond b3 to b1 inside the interphase itself. The boundary between regions I and II is unimportant, while the boundary between regions II and III occurs at $E_i = E_m$.

We expect the location of the boundaries between the different modes of failure in Fig. 9a and b to vary with the ratio of the cohesive energies $U_f/U_m$, since the OFMR itself is a function of the cohesive energy ratio [42]. However, the boundary $E_i = E_m$ in Fig. 9c does not contain any cohesive energy ratio dependence, and it is important to verify that it is truly independent of $U_f/U_m$. Fig. 10 shows the critical aspect ratio as a function of $E_f/E_i$ for a system with $E_f/E_m = 31.1$, $U_f/U_m = 1.5$ (full triangles) and 2.5 (full squares) compared to $U_f/U_m = 2$ (full circles). The OFIR does not vary significantly with cohesive energy ratio ($E_f/E_i \simeq 28$–$30$), but the flatness of the critical aspect ratio curve as well as the minimum critical aspect ratio itself are strongly influenced by the cohesive energy ratio. We find that for all three selected values of $U_f/U_m$ failure is initiated in the interphase shear bond b3 for $E_f/E_i \geq E_f/E_m$, while failure is initiated in the matrix tensile bond b4 for $E_f/E_i < E_f/E_m$. The failure analysis presented in Fig. 9c is therefore independent of the cohesive energy ratio $U_f/U_m$.

The above failure analysis provides useful information, especially for composites whose fibre–matrix modulus ratio is greater than the OFMR. This category encompasses the polymer composites, which are of considerable interest. Our computer results show that for these composites, with an interphase diameter several times the fibre diameter, there is no advantage

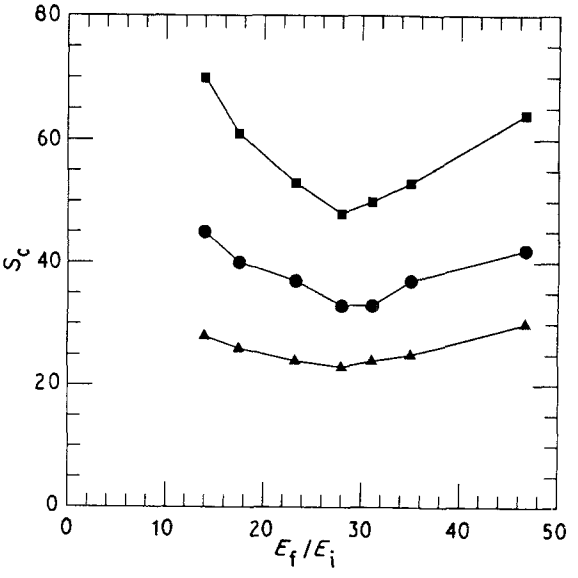


*Figure 10* Plot of the critical aspect ratio $S_c$ versus fibre–interphase modulus ratio $E_f/E_i$ for the system $E_f/E_m = 31.1$ for the following values of the fibre–matrix cohesive energy ratio: $U_f/U_m =$ (▲) 1.5, (●) 2 and (■) 2.5. The $y$ axis is in units of $1/d_f^w = 14.9/a_0^x$, where $a_0^x$ is a unit length in the $x$ direction. The solid lines do not represent a fit, but are added to help visualize the data.

in terms of a significant decrease in the critical aspect ratio to be gained by a proper choice of the interphase modulus alone. The above failure analysis suggests an alternate way to decrease the critical aspect ratio. The interphase modulus may be chosen such that failure shifts from the matrix to the interphase, and then another parameter can be brought into play: the interphase cohesive energy. The following section shows computer results for the dependence of the critical aspect ratio on the interphase cohesive energy.

## 3.2. Interphase cohesive energy

It is important to mention that one should keep in mind that a constant bond cohesive energy $U_\alpha$ generally implies a failure stress which increases with the bond elastic modulus and a failure strain which decreases with the bond elastic modulus. Increasing the cohesive energy of a bond implies increasing its stress and strain at failure, hence in this work toughness and strength are directly related to one another. For instance, a bond carrying tensile stress implies a (tensile) failure stress $\sigma_\alpha^*$ which varies as the square root of the bond elastic modulus $E_\alpha$, and varying the cohesive energy of the bond itself implies varying the (tensile) failure stress as the square root of the cohesive energy for a fixed bond elastic modulus, i.e. $\sigma_\alpha^* = (2E_\alpha U_\alpha)^{1/2}$ and the failure strain $\varepsilon_\alpha^* = (2U_\alpha/E_\alpha)^{1/2}$. In order to study the influence of interphase cohesive energy, we selected three out of the five systems chosen in the previous section namely, $E_f/E_m = 4$ as an example of low fibre–matrix modulus ratio, $E_f/E_m = 6$ as an example of a fibre–matrix modulus ratio in the vicinity of the OFMR, and $E_f/E_m = 31.1$ as an example of high fibre–matrix modulus ratio. Fig. 11 displays the critical aspect ratio versus fibre–interphase modulus ratio $E_f/E_i$ for these three cases for five different values of the interphase cohesive energy, $U_i = 0.8U_m$, $0.9U_m$, $U_m$, $1.2U_m$ and $1.5U_m$. Keeping in mind that the regions of interphase failure in Fig. 9a–c occur for $E_f/E_i \leq$ OFMR, $E_f/E_m \geq$ OFMR (with the OFMR between the values 8 and 14, according to Fig. 5) and $E_f/E_i \geq E_f/E_m$, respectively, the results in Fig. 11a–c demonstrate the sensitivity of the critical aspect ratio to the interphase cohesive energy when the fibre–interphase modulus ratio is in the region where interphase failure occurs (region II in Fig. 9a–c).

The critical aspect ratio in Fig. 11a–c decreases as the interphase cohesive energy $U_i$ increases. However, the interphase cohesive energy has little or no effect for a fibre–interphase ratio $E_f/E_i$ for which failure occurs in the matrix region: regions I and III in Fig. 9a–c. Note that the case $E_f/E_m = 31.1$ in Fig. 11c presents a peculiarity: the critical aspect ratio depends inversely on the interphase cohesive energy in the region of matrix failure, i.e. for $E_f/E_i < E_f/E_m$. This behaviour can be explained by the fact that upon fracture of bonds b5 (see Fig. 2), a greater amount of stress is redistributed in the neighbouring bonds for the case of a high-modulus fibre with a high-modulus interphase ($E_f/E_m$ large and $E_f/E_i$ low) than for the case of a more

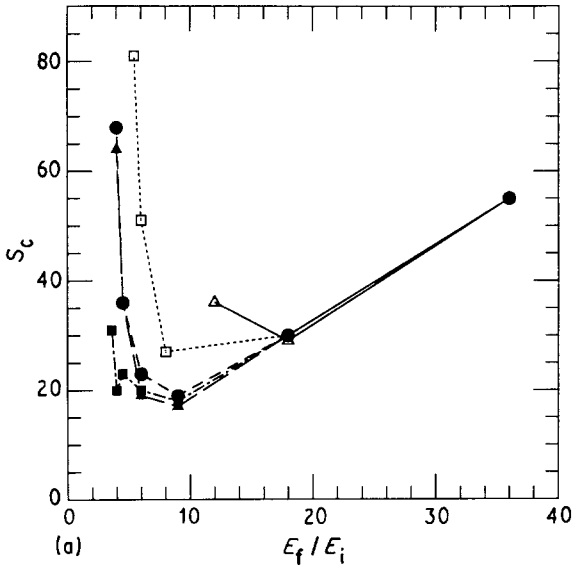


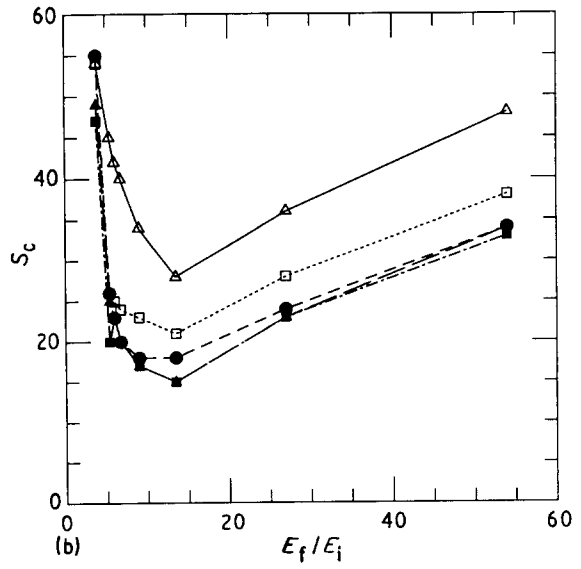


*Figure 11* Plots of the critical aspect ratio $S_c$ versus fibre-interphase modulus ratio $E_f/E_i$ for $U_i = (\triangle, ——)\ 0.8U_m, (\square, \cdots)\ 0.9U_m, (\bullet, - - -)\ U_m, (\blacktriangle, ——)\ 1.2U_m$ and $(\blacksquare, —\cdot—)\ 1.5U_m$; (a) is for a fibre–matrix modulus ratio $E_f/E_m = 4$, (b) for $E_f/E_m = 6$ and (c) for $E_f/E_m = 31.1$. The $y$ axis is in units of $1/d_f^w = 14.9/a_0^x$, where $a_0^x$ is a unit length in the $x$ direction. The lines do not represent a fit, but are added to help visualize the data.

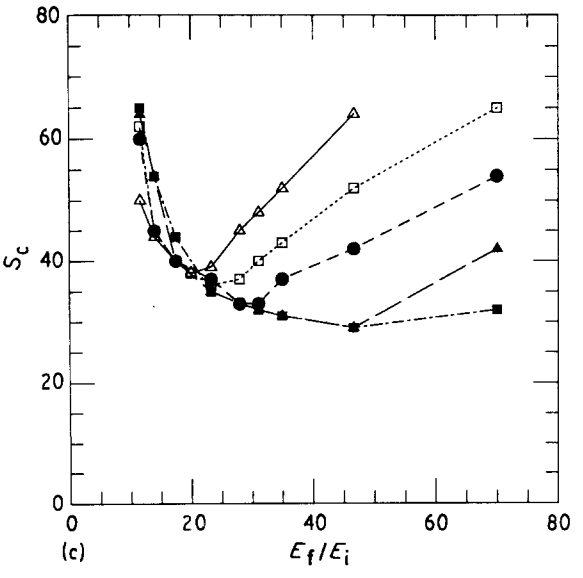

compliant fibre ($E_f/E_m$ lower). Moreover, it is also observed in the computer simulations that the debonding of high-modulus fibres (failure of bonds b5) with interphases which possess a high modulus $E_i$ and cohesive energy $U_i$ causes immediate failure in the (brittle) composite, at the same value of applied strain. This is not the case for the more compliant fibres where the fibre always debonds well before composite failure. Hence the fibre length must be increased for systems with a high value of $E_f/E_m$ (high-modulus fibres), a high value of $U_i$ (high interphase toughness and strength) and a low value of $E_f/E_i$ (high-modulus interphase) so that the fibre is able to break simultaneously with the end bonds b5. The inverse is true for the same systems with a lower interphase cohesive energy. In this case, decreasing the interphase cohesive energy allows the end bonds b5 to break sooner, and hence the stress redistribution to take place sooner. This explains the slight decreases in critical aspect ratio observed for a decreasing interphase cohesive energy.

Fig. 12 shows the composite strain at failure $\varepsilon^*$ as a function of fibre–interphase modulus ratio $E_f/E_i$ for the three cases. The interphase cohesive energy is the same as in Fig. 11. Fig. 12 is strongly correlated with Fig. 11, where one can see that the strain at failure increases with interphase cohesive energy for a fibre–interphase ratio such that failure occurs in the interphase according to Fig. 9: $E_f/E_i \leq$ OFMR for Fig. 12a, $E_f/E_i \geq$ OFMR for Fig. 12b and $E_f/E_i \geq E_f/E_m$ for Fig. 12c.

The optimum conditions for critical aspect ratio and composite strain at failure for fibre systems whose fibre–matrix modulus ratio is low are obtained for an interphase whose modulus is such that the fibre–interphase modulus ratio $E_f/E_i$ is close or equal to the OFMR in Fig. 5. This gain in load transfer efficiency might constitute an alternative to increasing the toughness of metal-matrix composites. The stress level in the matrix is reduced, as an increased amount of load is transferred to the fibre, for an interphase modulus $E_i \simeq E_f/\text{OFMR}$, compared to an interphase with modulus $E_i \gg E_f/\text{OFMR}$ (i.e. $E_i = E_m$) or $E_i \ll E_f/\text{OFMR}$. This increased load transfer efficiency as $E_i \to E_f/\text{OFMR}$ will cause the yield point of the metal matrix to occur at a larger value of applied strain ($\varepsilon > \varepsilon_{yield}$): as the matrix stress level is reduced due to an increased load transfer efficiency, the matrix stress would then reach its yield point for an applied strain $\varepsilon > \varepsilon_{yield}$. Therefore, this effect may be substantial enough so that an increased load transfer efficiency might represent a direction worth pursuing in order to increase the toughness of certain metal-matrix composites.

The condition $U_i > U_m$ only brings in a marginal improvement for composites with $E_f/E_i =$ OFMR. The interphase cohesive energy has little effect on systems with a ratio $E_f/E_i \geq$ OFMR (matrix failure). However, systems with more compliant interphases $E_f/E_i <$ OFMR (interphase failure) show a significant decrease in the critical aspect ratio (up to a factor of 4),

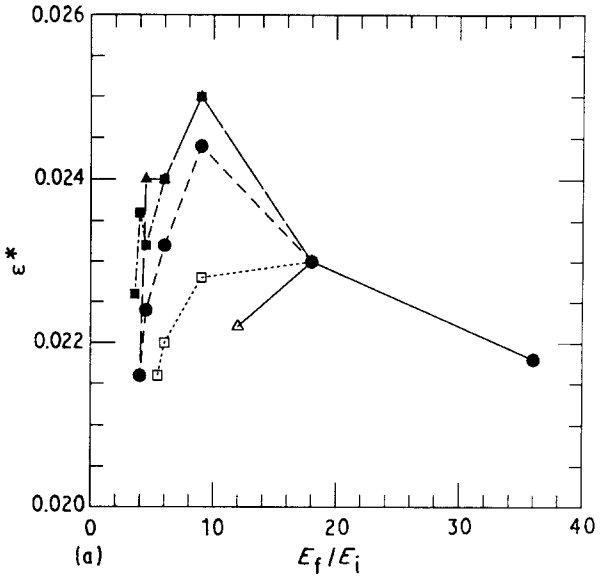


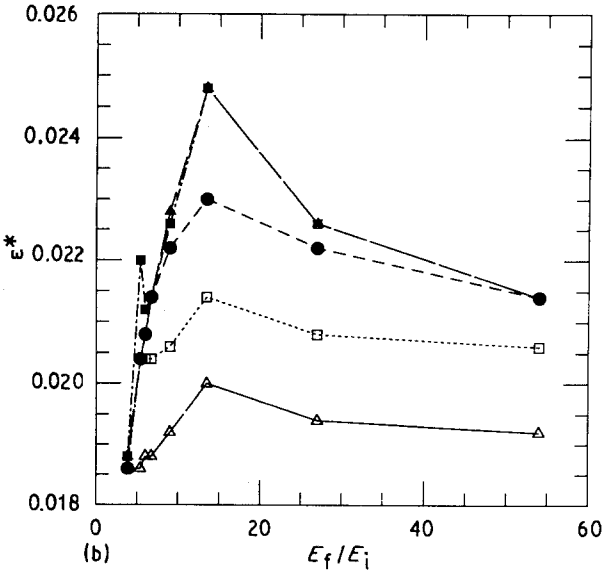


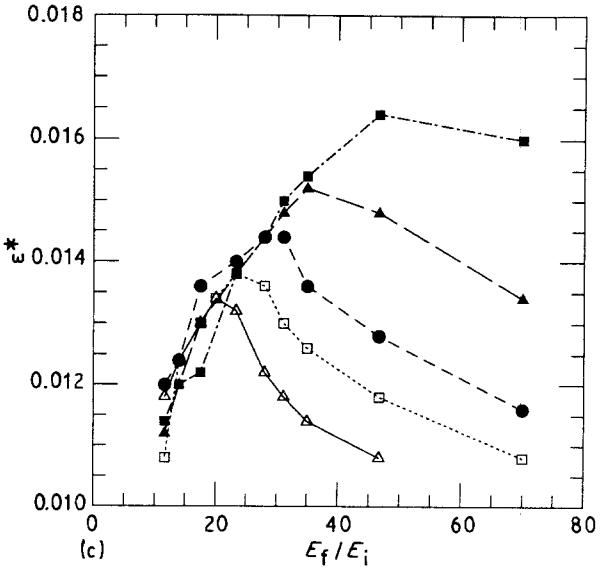


*Figure 12* Plot of the composite strain at failure ($\varepsilon^*$) versus fibre–interphase modulus ratio $E_f/E_i$ for $U_i = (\triangle, ——) 0.8U_m$, ($\square$, ···) $0.9U_m$, ($\bullet$, – – –) $U_m$, ($\blacktriangle$, ——) $1.2U_m$ and ($\blacksquare$, —·—) $1.5U_m$; (a) is for a fibre–matrix modulus ratio $E_f/E_m = 4$, (b) for $E_f/E_m = 6$ and (c) for $E_f/E_m = 31.1$. The $y$ axis is in units of $1/d_f^w = 14.9/a_0^x$, where $a_0^x$ is a unit length in the $x$ direction. The lines do not represent a fit, but are added to help visualize the data.

as well as a marginal increase in the composite strain at failure.

The optimum conditions for critical aspect ratio and composite strain at failure for a fibre system whose fibre–matrix modulus ratio is close or equal to the OFMR in Fig. 5 (i.e. $6 \leq E_f/E_m \leq 9$) are obtained for an interphase with a ratio $E_f/E_i$ also close or equal to the OFMR and $U_i > U_m$. The interphase cohesive energy has less effect on the critical length (up to a factor of 2.5) but more effect on the composite strain at failure compared to the previous case, for systems whose ratio $E_f/E_i$ is greater than or equal to the OFMR (interphase failure). One can also note a marginal improvement in both the critical aspect ratio and the composite strain at failure as the interphase cohesive energy is increased for systems with $E_f/E_i <$ OFMR (matrix failure).

The optimum conditions for critical aspect ratio and composite strain at failure for fibre systems whose fibre–matrix modulus is high is obtained for an interphase whose modulus $E_i$ is less than the matrix modulus $E_m$ and $U_i > U_m$. These composites are sensitive to interphase cohesive energy in the region $E_i \leq E_m$ (interphase failure), and the improvement in the critical length is comparable if not slightly less than in the previous case (up to a factor of 2). The composite strain at failure increases with interphase cohesive energy, especially in the region $E_i \leq E_m$, and the improvement is better than in the two previous cases.

The trends in the above results can be summarized as follows. Load transfer in systems with low $E_f/E_m$ is not very efficient, and decreasing the interphase modulus $E_i$ can substantially improve the load transfer and the critical length. Increasing the interphase cohesive energy $U_i$ has the same effect on the critical length: both factors $E_i$ and $U_i$ act together to decrease the critical length. In composites with a high ratio $E_f/E_m$, load transfer become worse upon decreasing the interphase modulus $E_i$, and stress amplification problems in the matrix prevent increasing the interphase modulus beyond the matrix modulus. One needs to decrease the interphase modulus so that the location of failure is shifted into the interphase, consequently both factors $E_i$ and $U_i$ compete against each other. However, the decreasing effect on the critical length of an increased interphase cohesive energy dominates. The effect of interphase cohesive energy on composite strain at failure is more important for systems with a high modulus ratio $E_f/E_m$ than for systems with a low modulus ratio, because a composite with a low value of $E_f/E_m$ has a strain at failure already close to the failure strain of the pure matrix and any additional gains are only marginal. In contrast, a high elastic modulus mismatch considerably embrittles the composite $\varepsilon_c^* \ll \varepsilon_m^*$ and in this case the gain in composite strain at failure due to increased interphase toughness can be quite substantial.

The results from the computer model suggest a strategy for improving the performance of composite materials. This strategy for an improved critical aspect ratio generally favours an interphase modulus less than the matrix modulus or at most equal, for ceramic-matrix and metal-matrix composites. Further improvement can be obtained by tailoring the interphase and providing it with additional energy-absorbing mechanisms. In addition, for polymer composites, decreasing the interphase modulus for interphases such that $d_i > d_f$ will be successful in optimizing the critical aspect ratio only if the interphase region (for $d_i \gg d_f$) is further tailored as to increase its energy absorbed at failure.

## 3.3. Interphase thickness

The above analysis in sections 3.1 and 3.2 is for an interphase whose diameter is much greater than the fibre diameter: we estimated $d_i/d_f$ to be approximately between 6 and 25 (see section 3.1). Theorcaris and Papanicolaou [45] showed that the interphase possesses a considerable thickness. This interphase may be due to various factors such as chemical reactions, or manufacturing processes occurring at the fabrication stage [46]. For instance, in many metal-matrix composite systems, the matrix chemically interacts with the fibre, producing a mesophase whose thickness generally depends on the cooling rate (e.g. [47]). An interphase whose thickness is much larger than the fibre thickness is not unreasonable. In polypropylene systems, transcrystalline interphases with diameter up to seven times the fibre diameter can be grown [48]. This last section proposes to estimate the effect of interphase thickness on the results reported in sections 3.1 and 3.2.

Fig. 13 shows the critical aspect ratio versus $E_f/E_i$ for an interphase thickness $d_i/d_f \simeq 12$–50, i.e. double the size of the interphase considered in sections 3.1 and 3.2 for the fibre–matrix systems $E_f/E_m = 4$ (full triangles, dotted line) and 31.1 (full squares, short dashed line). The cohesive energy ratio $U_f/U_m$ is 2 and

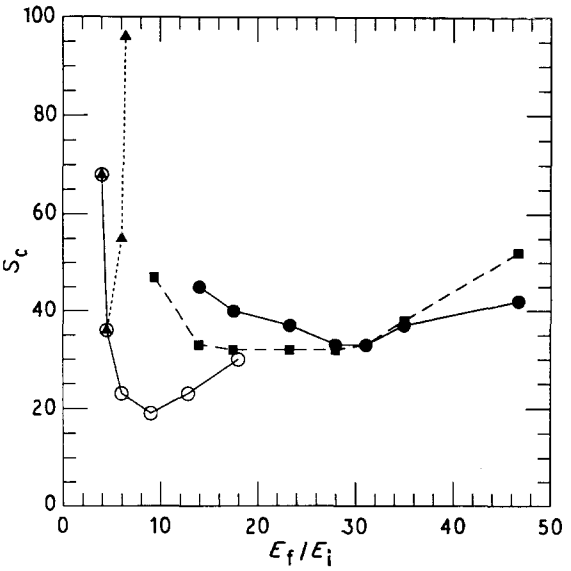


*Figure 13* Plot of the critical aspect ratio $S_c$ as a function of the fibre–interphase modulus ratio $E_f/E_i$ with $U_f/U_m = 2$, $U_i = U_m$ and $d_i/d_f \simeq 12$–50, for $E_f/E_m = (\blacktriangle, \ldots)$ 4 and $(\blacksquare, ---)$ 31.1. The data of Fig. 6 are also shown for comparison: $E_f/E_m = (\bigcirc)$ 4 and $(\bullet)$ 31.1. The $y$ axis is in units of $1/d_f^{\aleph} = 14.9/a_0^{\aleph}$, where $a_0^{\aleph}$ is a unit length in the $x$ direction. The lines do not represent a fit, but are added to help visualize the data.

$U_i = U_m$ in both systems. We also plot the critical aspect ratio measured in section 3.1 (Fig. 6) for $E_f/E_m = 4$ (open circles) and for $E_f/E_m = 31.1$ (full circles) joined by solid lines as a comparison. According to Fig. 13, we make the following two observations:

(i) A thick interphase with a modulus weaker than the matrix modulus eventually decreases the efficiency of load transfer for composites with a low fibre–matrix modulus ratio. The OFIR (which also represents the boundary between matrix and interphase failure) is shifted away from the OFMR, towards $E_f/E_m$.

(ii) Similarly, a thick interphase also reduces load transfer efficiency for composites with a high fibre–matrix modulus ratio and an interphase whose modulus is less than the matrix modulus (i.e. $E_f/E_i$ large). However, the thick interphase seems to modify the load transfer efficiency and failure mode for composites with interphases such that $E_f/E_i < E_f/E_m$. The critical aspect ratio curve to the left-hand side of $E_f/E_i = E_f/E_m$ flattens considerably and the location of failure shifts from the interphase shear bond b3 to the interphase tensile bond b1 instead of the matrix tensile bond b4 (see section 3.2). Considering the fact that the strain at failure is higher for the interphase $d_i/d_f \simeq 12$–$50$ than the interphase $d_i/d_f \simeq 6$–$25$, it seems plausible to assume that the smaller critical length found in Fig. 13 for $E_i > E_m$ is due to the fact that a thicker interphase smooths out the stress concentrations rather than improving the load transfer efficiency. Fig. 14a is a plot of the tensile stress profile along the fibre measured for an interphase modulus $E_i = 2.2E_m$, a fibre–matrix modulus ratio $E_f/E_m = 31.1$ and a fibre length $L = 33$ at 1.32% applied strain. The dotted line is for the interphase with $d_i/d_f \simeq 6$–$25$ while the short dashed line is for the interphase with $d_i/d_f \simeq 12$–$50$. The solid line represents the fibre failure stress $\sigma_f^* = (2E_f U_f)^{1/2}$. Fig. 14a shows that the stress transfer is not significantly different (slightly reduced) for the case of the thicker interphase $d_i/d_f \simeq 12$–$50$.

Fig. 14b shows the tensile stress profile along the first row above the fibre (interphase bonds between the matrix bonds b4 on Fig. 2 including the matrix bonds b4 themselves). The dotted line is for the interphase $d_i/d_f \simeq 6$–$25$ while the dot–short dashed line is for the interphase $d_i/d_f \simeq 12$–$50$. Fig. 14b also shows the tensile stress profile along the second row above the fibre: all matrix bonds between the bonds b2 in Fig. 2, including the bonds b2 themselves (matrix) plus two matrix bonds to the right of the rightmost bond b2 and to the left of the leftmost bond b2 for $d_i/d_f \simeq 10$–$25$ (short dashed line), and all interphase bonds between the two bonds b2 in Fig. 2, including the bonds b2 themselves (interphase) plus two matrix bonds to the right of the rightmost bond b2 and to the left of the leftmost bond b2 for $d_i/d_f \simeq 12$–$50$ (solid

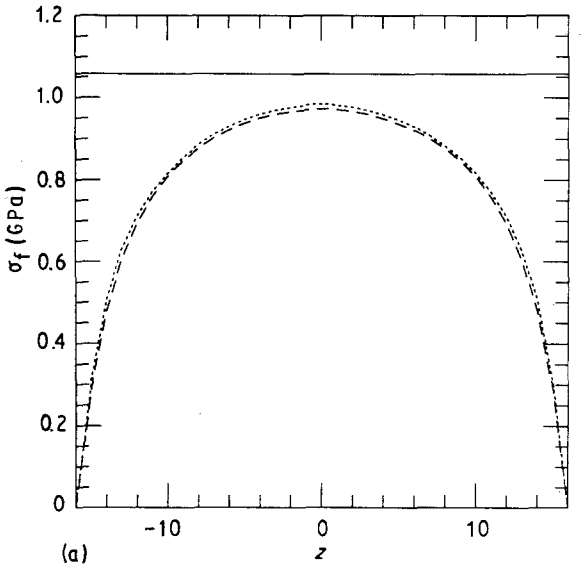


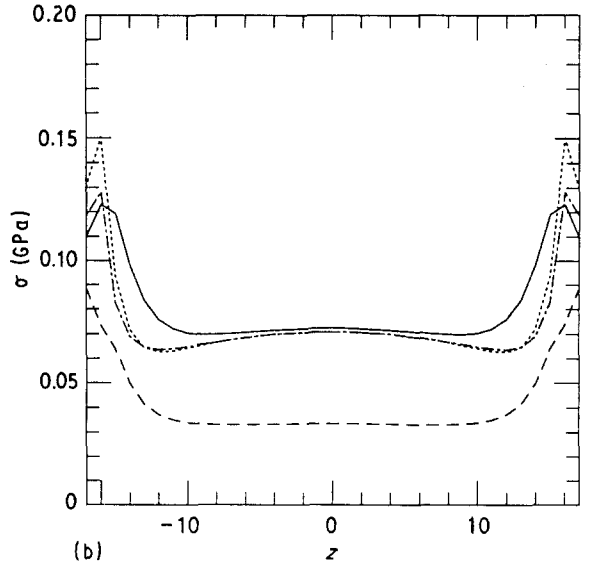


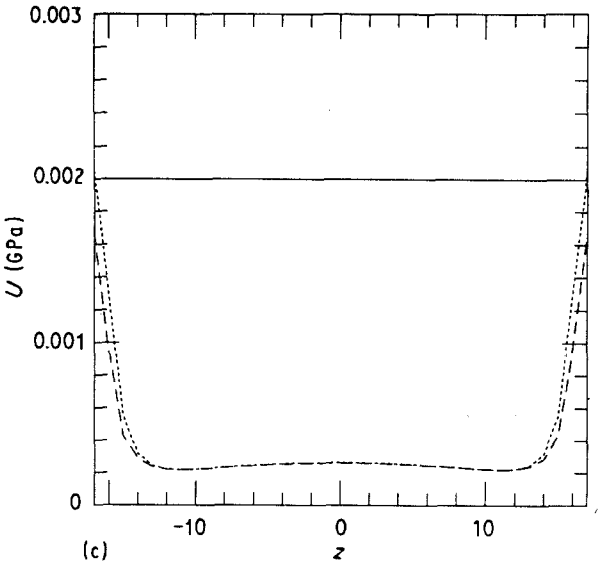


*Figure 14* (a) Tensile stress profile along the fibre (see Fig. 3a) for an interphase modulus $E_i = 2.2E_m$, ratios $E_f/E_m = 31.1$ and $U_f/U_m = 2$, fibre length $L = 32$ at 1.32% of applied strain, for $d_i/d_f \simeq$ (···) 6–25 and (– – –) 12–50; (——) fibre failure threshold. (b) Tensile stress profile ($\sigma$) of the bonds along the first and second row of nodes above the fibre, for $d_i/d_f \simeq$ (···, – – –) 6–25 and (——, —·—) 12–50. (c) Plot of the energy, $U$ stored in the tensile bonds along the first row of nodes above the fibre, for $d_i/d_f \simeq$ (···) 6–25 and (– – –) 12–50; (——) failure threshold $U_i = U_m$ of the matrix and interphase.

line). Fig. 14b displays a larger tensile stress amplification in the matrix bond b4 (located at $z = -17$ in Fig. 14b) in the case of the thinner interphase. A thicker interphase redistributes the stresses so they are more uniform: the stress in bonds b1 and b4 (first row, see Fig. 2) decrease, but the stress in the bonds above b1 and b4 increase (second row, see Fig. 2). Fig. 14c is a plot of the energy stored in the bonds along the first row above the fibre (same bonds as in Fig. 14b). The solid line represents the failure threshold of the matrix and interphase $U_i = U_m$. Fig. 14c confirms that the matrix tensile bond b4 is slightly above the failure point in the case of $d_i/d_f \simeq 6$–25 (dotted line), while for the thicker interphase, the matrix bond b4 is well below the failure threshold (short dashed line).

Keeping in mind the results of Fig. 11c in section 3.2, i.e. that for composites with a high fibre–matrix modulus ratio and a stiff interphase the critical length decreases with decreasing interphase cohesive energy, it has also been verified that decreasing the cohesive energy of the thicker interphases also results in a decrease of the critical length. However, the gain found compared to the case $U_i = U_m$ is only marginal. For the system $E_f/E_m = 31.1$ with an interphase such that $E_f/E_i = 23$, 17.5, 14 and 9, we obtained a decrease in the critical length of less than 10% for $0.5 \geq U_i/U_m \geq 0.95$. The critical length increases again for $U_i/U_m < 0.5$. We compare this result to the right-hand side of $E_f/E_i = 31.1$ in Fig. 11c, i.e. $E_i < E_m$, where the critical length is decreased by a factor of almost 50% upon an increase by a factor of 1.5 in cohesive energy. The above results seem to indicate a trend, i.e. thicker interphases can potentially reduce stress amplifications effects, for an interphase whose modulus is greater than the matrix modulus. On the other hand, it is expected that the thinner and stiffer is the interphase, the more it increases the stress amplification patterns at the fibre end-points.

## 4. Summary and conclusions

This work studied the effect of interphase modulus and cohesive energy on the critical aspect ratio in short-fibre composites. The only case where the interphase modulus has a strong effect on load transfer for a constant interphase cohesive energy $U_i = U_m$ is found for composites with a low fibre–matrix modulus ratio, i.e. metal-matrix and ceramic-matrix composites, whose modulus ratio is less than the OFMR identified in previous work [42]. The interphase modulus for which the minimum critical aspect ratio is achieved is such that $\text{OFIR} = E_f/(E_i)_{opt} = \text{OFMR}$. The value for this optimum interphase modulus $(E_i)_{opt}$ increases towards the value for the matrix modulus as the composite fibre–matrix modulus ratio increases towards the OFMR. Composites whose fibre–matrix modulus ratio is greater than the OFMR, such as the polymer composites, display a minimum critical aspect ratio for the perfect interphase $E_i = E_m$ and $U_i = U_m$, independently of the fibre–matrix cohesive energy ratio $U_f/U_m$ chosen. This result is explained by the fact that, in spite of an increased load transfer efficiency with increasing interphase modulus, the stress amplification generated in the matrix causes an embrittlement of the composite: the composite fails at a value of applied strain much lower than for the perfect interphase.

We identified various failure regions and failure modes as a function of the interphase modulus. We found a substantial effect of interphase cohesive energy on the critical aspect ratio of polymer composites, for interphase moduli such that failure is located in the interphase itself. An effect of cohesive energy on critical aspect ratio was also found for metal-matrix and ceramic-matrix composites, and this effect can be more considerable than for the polymer composites. These results suggest a strategy for tailoring interphases in polymer composites, which favours an interphase with a modulus weaker than the matrix, but able to sustain a higher strain at failure than the matrix (higher cohesive energy).

We examined the effect of interphase thickness on the above results. It was found that a thicker interphase decreases the critical aspect ratio in polymer composites with interphases whose moduli $E_i > E_m$. This result is not due to an increased load transfer efficiency with interphase thickness, but to the fact that a thicker interphase is able to redistribute the stress amplifications in the matrix. This finding seems to indicate that thin interphases have a potential for composite embrittlement, as compared to thicker interphases.

Future work is planned in which the present methodology can be modified so as to include anisotropies in the interphase region and viscous interactions, before undertaking the study of multi-fibre composites.

## References


1. M. R. PIGGOTT, in "Load Bearing Fibre Composites" (Pergamon, Oxford, 1980).
2. M. J. OWEN, in "Fracture and Fatigue", edited by L. J. Broutman (Academic, New York, 1974) p. 341.
3. J.-H. KIM and Y.-W. MAI, *Compos. Sci. Tech.* **41** (1991) 333.
4. E. MÄDER and K. H. FREITAG, *Composites* **21** (1990) 397.
5. J. P. FAVRE and J. PERRIN, *J. Mater. Sci.* **7** (1972) 1113.
6. J. P. FAVRE and M. C. MERRIENE, *Int. J. Adhesion Adhesives* **1** (1981) 311.
7. L. ONGCHIN, W. K. OLENDER and F. H. ANCKER, in 27 Ann. Tech. Comp. SPI, Section 11A (1972) 27.
8. V. RAO and L. T. DRZAL, *Polym. Compos.* **12**(1) (1991) 48.
9. B. MILLER, P. MURI and L. REBENFELD, *Compos. Sci. Tech.* **28** (1987) 17.
10. J. F. MANDELL, D. H. GRANDE, T.-H. TSIANG and F. J. McGARRY, in Proceedings of 7th International Conference on Composite Materials (American Society for Testing and Materials, Philadelphia, 1986) p. 87.
11. H. C. TSAI, A. M. AROCHO and L. W. GAUSE, *Mater. Sci. Engng* **A126** (1990) 295.
12. M. K. TSE, *SAMPE J.* **21**(5) (1985) 11.
13. P. HERRERA-FRANCO, W.-L. WU, M. MADHUKAR and L. T. DRZAL, in Proceedings of 46th Annual Conference of Composites Institute (Society of the Plastics Industry, 1991) p. 18.
14. M. R. PIGGOTT, in Proceedings of 36th International SAMPE Symposium (1991) p. 1773.
15. I. VERPOAEST, M. DESAEGER and R. KEUNINGS, in "Controlled Interphases in Composite Materials", Proceedings of 3rd International Conference on Composite Interfaces (ICCI-III), edited by Hatsuo Ishida (Cleveland, Ohio, 1990) p. 653.

16. M. R. PIGGOTT, *Compos. Sci. Tech.* **30** (1987) 295.
17. T. F. COOKE, *J. Polym. Engng* **7** (1987) 197.
18. G. J. SPIES, *J. Aircraft Eng.* **25** (1953) 64.
19. J. J. BIKERMAN, *J. Appl. Phys.* **28** (1957) 1484.
20. N. ARAVAS, K. S. KIM and M. J. LOUKIS, *Mat. Sci. Engng* **A107** (1989) 159.
21. K. S. KIM and N. ARAVAS, *Int. J. Solid Struct.* **24** (1988) 417.
22. K. KENDALL, *J. Adhesion* **5** (1973) 105.
23. M. NARDIN and J. SCHULTZ, *C. R. Acad. Sci. Paris*, **311** (II) (1990) 613.
24. E. M. ASLOUN, M. NARDIN and J. SCHULTZ, *J. Mater. Sci.* **24** (1989) 1835.
25. H. L. COX, *Br. J. Appl. Phys.* **3** (1952) 72.
26. K. KENDALL, *J. Mater Sci.* **10** (1975) 1011.
27. B. W. ROSEN, in "Fibre Composite Materials" (American Society for Metals, Ohio, 1965).
28. N. F. DOW, Report TIS R635D61 (General Electric Co., 1963).
29. W. ROSEN, *AIAA J.* **2** (1964) 1985.
30. A. KELLY and G. J. DAVIES, *Metall. Rev.* **10** (37) (1965).
31. W. R. TYSON and G. J. DAVIES, *Br. J. Appl. Phys.* **16** (1965) 199.
32. M. R. PIGGOTT, *Acta Metall.* **14** (1966) 1429.
33. H. D. WAGNER and A. EITAN, *Appl. Phys. Lett.* **56** (1990) 1965.
34. N. C. REMEDIOS and W. G. WOOD, *J. Compos. Mater.* **2** (1968) 517.
35. A. S. CARRARON and F. J. McGARRY, *ibid.* **2** (1968) 222.
36. J. HARNER and N. ASHBAUGH, Technical Report USAAVLABS-TR-67-66, AD-66790 (Wittaker Corporation, 1968).
37. G. C. SHIH and L. J. EBERT, *J. Compos. Mater.* **21** (1987) 207.
38. Y. TERMONIA, *J. Mater. Sci.* **25** (1990) 103.
39. P. S. THEORCARIS, *J. Appl. Polym. Sci.* **30** (1985) 621.
40. *Idem*, "The Mesophase Concept in Composites" (Springer, New York, 1987).
41. M. NARKIS, E. J. H. CHEN and R. B. PIPES, *Polym. Compos.* **9** (1988) 245.
42. L. MONETTE, M. P. ANDERSON, S. LING and G. S. GREST, *J. Mater. Sci.* **27** (1992) 4393.
43. D. HULL, in "An Introduction to Composite Materials" (Cambridge University Press, Cambridge, 1981).
44. D. M. SCHUSTER and E. SCALA, *Trans. Met. Soc. AIME* **230** (1965) 1491.
45. P. S. THEORCARIS and G. C. PAPANICOLAOU, *Fibre Sci. Technol.* (1979) 421.
46. S. K. CHATURVEDI and G. Y. TZENG, *Compos. Engng* **1** (1991) 49.
47. R. B. CLOUGH, F. S. BIANCANIELLO, H. N. G. WADLEY and U. R. KATTNER, *Met. Trans.* **21A** (1990) 2747.
48. A. LUSTIGER and D. WAGNER, Private communication **8** (1991).

*Received 3 September 1991*
*and accepted 30 March 1992*